

A consensus-constrained parsimonious Gaussian mixture model for clustering hyperspectral images

Ganesh Babu^{*1}, Aoife Gowen^{†2}, Michael Fop^{‡1}, and Isobel Claire Gormley^{§1}

¹School of Mathematics and Statistics,
²School of Biosystems and Food Engineering
 University College Dublin, Ireland.

Abstract

The use of hyperspectral imaging to investigate food samples has grown due to the improved performance and lower cost of spectroscopy instrumentation. Food engineers use hyperspectral images to classify the type and quality of a food sample, typically using classification methods. In order to train these methods, every pixel in each training image needs to be labelled. Typically, computationally cheap threshold-based approaches are used to label the pixels, and classification methods are trained based on those labels. However, threshold-based approaches are subjective and cannot be generalized across hyperspectral images taken in different conditions and of different foods. Here a consensus-constrained parsimonious Gaussian mixture model (ccPGMM) is proposed to label pixels in hyperspectral images using a model-based clustering approach. The ccPGMM utilizes available information on the labels of a small number of pixels and the relationship between those pixels and neighbouring pixels as constraints when clustering the rest of the pixels in the image. A latent variable model is used to represent the high-dimensional data in terms of a small number of underlying latent factors. To ensure computational feasibility, a consensus clustering approach is employed, where the data are divided into multiple randomly selected subsets of variables and constrained clustering is applied to each data subset; the clustering results are then consolidated across all data subsets to provide a consensus clustering solution. The ccPGMM approach is applied to simulated datasets and real hyperspectral images of three types of puffed cereal, corn, rice, and wheat. Improved clustering performance and computational efficiency are demonstrated when compared to other current state-of-the-art approaches.

1 Introduction

Hyperspectral imaging is a spectroscopic method combining digital imaging with spectroscopy (Gowen et al., 2019). Hyperspectral imaging collects an image as a function of the light, in which each pixel is a vector of reflectance or fluorescence information of the sample under study in the continuous spectrum. The idea behind producing hyperspectral images lies in the interaction between the photons emitted by a light source and the physical and chemical properties of the sample (Amigo and Santos, 2020). The interaction allows hyperspectral images to capture critical information and traits of a sample not visible to the naked eye. The critical information captured on the continuous spectrum can be affected by spatial interference and spectral and redundant noise (Amigo, 2020). These issues are effectively handled with computationally intensive spectral preprocessing techniques (Amigo, 2010) like denoising and scatter correction (Rinnan et al., 2009; Bocklitz et al., 2011; Geladi et al., 1985). The preprocessed information is then used to detect chemical contamination, adulteration, and presence of foreign components in the food samples under study (Feng and Sun, 2012). Thanks to the increasing availability of statistical methods for handling complex data, food engineers are routinely employing classification

*ganesh.babu@ucdconnect.ie

†aoife.gowen@ucd.ie

‡michael.fop@ucd.ie

§claire.gormley@ucd.ie

Isobel Claire Gormley and Michael Fop contributed equally to this work.

methods for segmentation, food sample detection, and analysis of large volumes of hyperspectral food images.

To train a classification method, each pixel of a hyperspectral image needs to be appropriately labelled as e.g., either the background or the food sample. Usually, the images are captured on appropriate backgrounds that facilitate segmentation. In such cases, to select the regions of interest or the food sample under study, a process called masking is performed to remove the background pixels from the image (Amigo et al., 2015). To create the mask, multiple techniques are employed (Pal and Pal, 1993), with the most widely used being k -means clustering (Amigo et al., 2015) and threshold-based approaches (Pal and Pal, 1993; Gowen et al., 2019; Xu et al., 2020). In Amigo et al. (2015), k -means clustering with 2 clusters is applied to a set of hyperspectral images to separate the background from the food sample. Abdi and Williams (2010), Gowen et al. (2019), and Xu et al. (2020) highlight some of the prominent threshold-based approaches used to label the different food samples and background pixels in a given hyperspectral image. In threshold-based approaches, the threshold for the segmentation of the pixels is selected by producing a histogram of some useful pixel-related summary of the entire spectrum, like the mean or the principal component scores of the wavelength intensities for each pixel. The selection of which summary to employ in the histogram depends on the type of background and the food sample under study. In the histogram, typically a bimodal distribution is observed and a threshold is subjectively chosen as the point that separates the two modes. The quality of the threshold inferred labels in each hyperspectral image depends on several decisions like the summary metric used and which variables are selected for computing the summary. Furthermore, with the threshold approach, only hard classification of pixels as background or food type are possible, ignoring the inherent uncertainty in the labelling process, particularly in certain areas of the image, like the pixels around the edges of the food sample (Amigo and Santos, 2020).

A major challenge in labelling the pixels of the hyperspectral images is that each image has a large number of pixels and for each pixel, a large amount of reflectance information is captured in a continuous p -dimensional spectrum, whose wavelengths are highly correlated. Further, often threshold and k -means clustering approaches are applied to each hyperspectral image individually, which is impractical as the number of images increases and does not allow for the borrowing of information across images. Also, the threshold approach and k -means clustering with 2 clusters work well only when there is exactly one type of food sample in a hyperspectral image. As the number of food samples in a given image increases, multiple thresholds need to be selected from the histogram, which is even more challenging. Overall, threshold based approaches are subjective and are not easily generalisable across hyperspectral images.

Approaches to clustering pixels in hyperspectral images are receiving increasing attention (Zhai et al., 2021). The density based DBSCAN clustering approach (Khan et al., 2014; Hahsler et al., 2019) has been widely used in imaging. Further, model-based clustering approaches have proved effective, for example via Gaussian mixture models (GMM, Scrucca et al., 2016; McNicholas, 2016; Bouveyron et al., 2019) and parsimonious versions (McNicholas and Murphy, 2008). Bouveyron and Brunet-Saumard (2014) propose a dimension reduction-based approach to segmenting hyperspectral images of Mars. Further, Jacques and Ruckebusch (2016) consider co-clustering of pixels and wavelengths in the context of hyperspectral imaging of an oil-in-water emulsion using a latent block model.

Here, we propose a novel model-based clustering approach, a consensus-constrained parsimonious Gaussian mixture model (ccPGMM), to label the pixels of multiple hyperspectral images simultaneously in a computationally feasible manner while accounting for uncertainty. A key aspect of ccPGMM is that it involves a constrained parsimonious Gaussian mixture model (Melnykov et al., 2016) in which information regarding the types of food samples present in the hyperspectral images along with information about some pixels is incorporated as constraints to perform informed clustering. Further, as hyperspectral images have a large number of pixels, each of which has an associated high-dimensional spectrum of p strongly correlated variables, ccPGMM employs a parsimonious Gaussian mixture model (PGMM) which describes the high-dimensional data using a small number of latent variables. To enable computationally efficient implementation, ccPGMM adopts a consensus approach, whereby the high-dimensional spectrum is divided into randomly selected subsets of $d < p$ variables, and a constrained PGMM is fitted to each subset of variables on all pixels. The clustering solutions of the constrained PGMMs fitted to each subset are consolidated to provide a final consensus clustering allocation for each pixel. The performance of the proposed ccPGMM approach is demonstrated, and compared to other state-of-the-art approaches, through thorough simulation studies and application

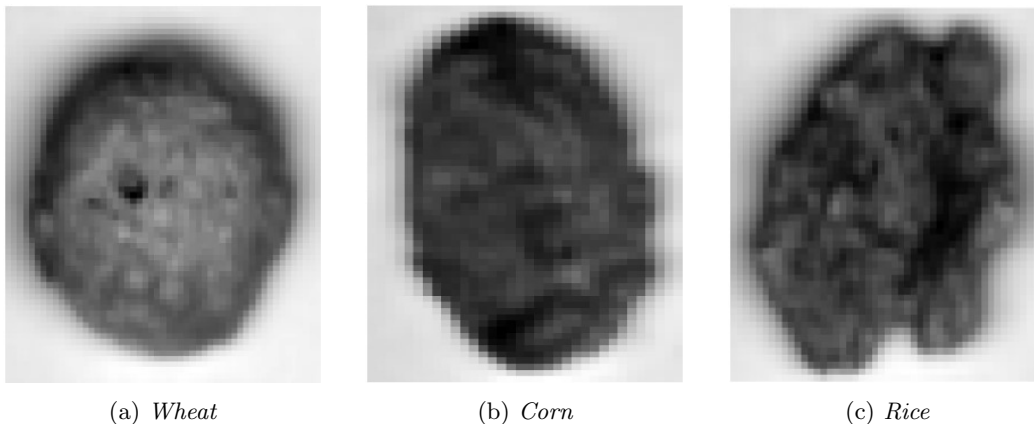


Figure 1: *Greyscale images of one hyperspectral image of each puffed cereal type. For each pixel, the intensity of the color corresponds to the average of its NIR spectrum.*

to real hyperspectral images of puffed cereals (Gowen et al., 2019).

In what follows, Section 2 gives details of the motivating dataset containing hyperspectral images of puffed cereals. Section 3 outlines the ccPGMM approach and discusses its inference and implementation details. Section 4 delineates thorough simulation studies that explore the performance of ccPGMM under different settings. Section 5 discusses the application of ccPGMM to the motivating puffed cereal images and Section 6 summarises the contributions of ccPGMM and gives an overview of future research directions. The R (R Core Team, 2023) code to implement ccPGMM is available at this repository [GitHub](#).

2 Hyperspectral images of puffed cereals

The ccPGMM approach is motivated by the need to simultaneously label pixels in nine hyperspectral images of three types of puffed cereal, wheat, corn, and rice (Gowen et al., 2019). Each pixel in an image records the near-infrared (NIR) spectrum, with $p = 101$ equally spaced variables spanning the wavelengths in the 880-1720nm interval. Each image $l = 1, \dots, L = 9$ contains only one puffed cereal and is a three-dimensional tensor of dimension $S_l \times T_l \times p$ where S_l and T_l are the numbers of row and column pixels respectively, which vary across the images as they are of different dimensions (details are given in Appendix 8). Figure 1 shows a greyscale image of one hyperspectral image of each puffed cereal type, where, for each pixel, the intensity of the color is given by the average of the NIR spectrum.

For the purpose of ccPGMM, the pixels are assumed to be independent and so the three-dimensional tensor of each image is represented by a rectangular dataset of dimension $(S_l T_l) \times p$. These $L = 9$ rectangular datasets are then collated to form a single dataset of dimension $N \times p$, where $N = \sum_{l=1}^L S_l T_l$. Here, the final dataset of nine images results in $N = 28039$ pixels, each measured over $p = 101$ wavelengths which are highly correlated and contain spectral noise.

The objective is to simultaneously label all pixels in all nine images as either background or a cereal type, taking into account available information on the images (i.e., it is known which cereal type is in each image) and on some pixels (e.g., corner pixels are background), in a computationally feasible manner.

3 The ccPGMM and its inference

3.1 Parsimonious Gaussian mixture models (PGMM)

Factor analysis is a latent variable model that represents a large number p of correlated variables using a smaller number $q \ll p$ of underlying latent factors. In a single factor analysis model (McLachlan and Peel, 2000), each observation $\mathbf{x}_n \in \mathbb{R}^p$ for $n = 1, \dots, N$ in data $\mathbf{X} = \{\mathbf{x}_1, \dots, \mathbf{x}_N\}$ of dimension $N \times p$ is modelled as $\mathbf{x}_n = \boldsymbol{\mu} + \boldsymbol{\Lambda} \mathbf{u}_n + \boldsymbol{\varepsilon}_n$ where $\boldsymbol{\mu}$ is the mean, $\boldsymbol{\Lambda}$ is the $p \times q$ loadings matrix and $\mathbf{u}_n \sim \mathcal{N}_q(\mathbf{0}, \mathbf{I})$ and $\boldsymbol{\varepsilon}_n \sim \mathcal{N}_p(\mathbf{0}, \boldsymbol{\Psi})$ are the latent factor score and specific factor, respectively, for

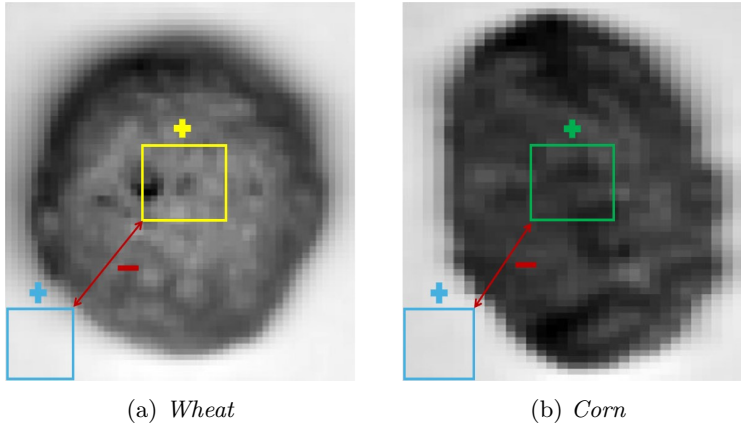


Figure 2: An illustration of positive (+) and negative (-) constraints. Four blocks of three types of pixels are highlighted. Pixels in the blue blocks (assumed to be the background) must be clustered together, as must the pixels in the yellow block (wheat) and the pixels in the green block (corn). However, pixels in the blue blocks must not be clustered with those in the yellow block or with those in the green block, and vice versa.

observation n . Therefore, $\mathbf{x}_n \sim \mathcal{N}_p(\boldsymbol{\mu}, \boldsymbol{\Sigma})$, where $\boldsymbol{\Sigma} = \boldsymbol{\Lambda}\boldsymbol{\Lambda}^\top + \boldsymbol{\Psi}$ provides a parsimonious covariance structure.

The parsimonious Gaussian mixture model (PGMM) (McLachlan and Peel, 2004; McNicholas and Murphy, 2008; McNicholas et al., 2010) is a finite mixture of G factor analysis models such that each mixture component g has a multivariate Gaussian distribution with mean $\boldsymbol{\mu}_g$ and covariance $\boldsymbol{\Lambda}_g\boldsymbol{\Lambda}_g^\top + \boldsymbol{\Psi}_g$. Denoting the probability of membership of mixture component g as τ_g , under PGMM, we have $f(\mathbf{x}_n) = \sum_{g=1}^G \tau_g \mathcal{N}_p(\mathbf{x}_n; \boldsymbol{\mu}_g, \boldsymbol{\Lambda}_g, \boldsymbol{\Psi}_g)$. By constraining $\boldsymbol{\Lambda}_g$ and $\boldsymbol{\Psi}_g$ to be the same or different across components, a family of PGMMs have been developed (McNicholas and Murphy, 2008) with inference via an alternating expectation-conditional maximization (AECM, Ghahramani et al., 1996; McLachlan et al., 2003). These PGMMs facilitate model-based clustering of high-dimensional data.

3.2 Constrained parsimonious Gaussian mixture models

When labelling pixels in a set of hyperspectral images, there is often information about the type of food sample(s) present in some of the hyperspectral images, along with indirect information on the labels of some pixels in the images. For example, in Figure 2, four blocks of pixels are highlighted in three different colours in the two images. The pixels in the blue blocks located at the corner of the images are assumed to belong to the background. On the other hand, the pixels in the yellow and green blocks are located in the center of their images, where the corresponding cereal is observed to be situated. Pixels in the blue blocks should be clustered together, as must the pixels in the yellow block and the pixels in the green block; this information imposes what are known as positive constraints. Also, the pixels in the blue blocks should not be placed in the same cluster as pixels in the yellow or green blocks, and vice versa; this information imposes what are known as negative constraints.

Melnykov et al. (2016) proposed a constrained Gaussian mixture model that uses such additional information about some observations as constraints to perform informed model-based clustering. However, the high-dimensionality of the hyperspectral imaging data poses computational challenges for this approach. Here, we build on Melnykov et al. (2016) and allow for constraints to be incorporated when clustering using a PGMM. The resulting constrained parsimonious Gaussian mixture model (constrained-PGMM) facilitates clustering and therefore labelling of the pixels of the hyperspectral images.

Under the constrained-PGMM, the observed data log-likelihood is

$$\ell_o(\mathbf{X}) = \sum_{n=1}^N \log \sum_{g=1}^G \tau_g \mathcal{N}_p(\mathbf{x}_n; \boldsymbol{\mu}_g, \boldsymbol{\Lambda}_g, \boldsymbol{\Psi}_g). \quad (1)$$

As (1) is difficult to maximize directly, an AECM algorithm is used to fit the constrained-PGMM.

This requires the introduction of a latent component indicator $\mathbf{z}_n = (z_{n1}, \dots, z_{nG})'$, for $n = 1, \dots, N$, where $z_{ng} = 1$ if observation n belongs to cluster g or 0 otherwise. The AECM algorithm works in two cycles and allows for a different definition of the complete data in each cycle. In the first cycle, the component indicators $\mathbf{Z} = \{\mathbf{z}_1, \dots, \mathbf{z}_N\}$ are assumed to be the missing data. The complete data log-likelihood is then

$$\ell_c(\mathbf{X}, \mathbf{Z}) = \sum_{n=1}^N \sum_{g=1}^G z_{ng} [\log \tau_g + \log \mathcal{N}_p(\mathbf{x}_n; \boldsymbol{\mu}_g, \boldsymbol{\Lambda}_g, \boldsymbol{\Psi}_g)]. \quad (2)$$

In the E-step of the first cycle, the available constraints are incorporated into PGMM. Let B_1 be the set of J pixels (indexed by j) in the blue blocks shown in Figure 2 which are known to be background and must be clustered together. Let B_2 be the set of O pixels (indexed by o) in the yellow block of Figure 2 which are known to be wheat and should be clustered together. These are positive constraints (denoted $+$). However, the pixels in B_1 should not be clustered together with the pixels in B_2 . This is a negative constraint (denoted $-$). Thus the posterior probability $\hat{z}_{B_1, g}^+$ of the pixels in B_1 belonging to cluster g , given the positive and negative constraints \pm is

$$\hat{z}_{B_1, g}^+ = \frac{\prod_{\substack{j \in B_1 \\ j=1}}^J \hat{\tau}_g \mathcal{N}_p(\mathbf{x}_j; \hat{\boldsymbol{\mu}}_g, \hat{\boldsymbol{\Lambda}}_g \hat{\boldsymbol{\Lambda}}_g^\top + \hat{\boldsymbol{\Psi}}_g) \sum_{\substack{f=1 \\ f \neq g}}^G \prod_{\substack{o \in B_2 \\ o=1}}^O \hat{\tau}_f \mathcal{N}_p(\mathbf{x}_o; \hat{\boldsymbol{\mu}}_f, \hat{\boldsymbol{\Lambda}}_f \hat{\boldsymbol{\Lambda}}_f^\top + \hat{\boldsymbol{\Psi}}_f)}{\sum_{g'=1}^G \prod_{\substack{j \in B_1 \\ j=1}}^J \hat{\tau}_{g'} \mathcal{N}_p(\mathbf{x}_j; \hat{\boldsymbol{\mu}}_{g'}, \hat{\boldsymbol{\Lambda}}_{g'} \hat{\boldsymbol{\Lambda}}_{g'}^\top + \hat{\boldsymbol{\Psi}}_{g'}) \sum_{\substack{f=1 \\ f \neq g'}}^G \prod_{\substack{o \in B_2 \\ o=1}}^O \hat{\tau}_f \mathcal{N}_p(\mathbf{x}_o; \hat{\boldsymbol{\mu}}_f, \hat{\boldsymbol{\Lambda}}_f \hat{\boldsymbol{\Lambda}}_f^\top + \hat{\boldsymbol{\Psi}}_f)}, \quad (3)$$

where $\hat{\cdot}$ denotes an initial or current parameter value, as relevant. In (3), the posterior probabilities of pixels in B_1 are considered with only one set of pixels B_2 as a negative constraint, however (3) can easily be extended to accommodate multiple such negative constraints. The remaining pixels in Figure 2 which are not in the highlighted blocks are considered as blocks with only one pixel and no negative constraints. The estimated model parameters $\hat{\boldsymbol{\mu}}_g$ and $\hat{\tau}_g$ are updated in the M-step of the first cycle as in PGMM (see [McNicholas and Murphy, 2008](#)). Further details are in Appendix 9.

In the E-step of the second cycle, the expected value of $\hat{z}_{B_1, g}^+$ is computed as in (3), with $\hat{\boldsymbol{\mu}}_g$ and $\hat{\tau}_g$ updated to those from the M-step of the first cycle. The expected value of \mathbf{u}_n , $n = 1, \dots, N$, and the estimates of $\hat{\boldsymbol{\Lambda}}_g$ and $\hat{\boldsymbol{\Psi}}_g$, $g = 1, \dots, G$ are computed as in PGMM; details are reported in Appendix 9.

The AECM algorithm moves between these cycles, iteratively updating the model parameters, until convergence. The values of $\hat{\mathbf{Z}}$ at convergence are the posterior probabilities of cluster membership for each pixel; labels can be obtained based, for example, on the *maximum a posteriori* values of $\hat{\mathbf{Z}}$. However, constrained-PGMM exhibits very long run times when fitted to the hyperspectral image data and could not be fitted to the entire $p = 101$ variables of the motivating dataset in a computationally efficient manner.

3.3 Consensus-constrained parsimonious Gaussian mixture models

To improve the computational efficiency of constrained-PGMM, we propose a consensus-constrained parsimonious Gaussian mixture model (ccPGMM), inspired by [Russell et al. \(2015\)](#). [Russell et al. \(2015\)](#) proposed a consensus approach to avoid the selection of a single best model based on the Bayesian information criterion (BIC, [Neath and Cavanaugh, 2012](#); [Schwarz, 1978](#)). In [Russell et al. \(2015\)](#), the clustering solutions of multiple models fitted on the same data are consolidated to provide the final consensus clustering solution. Previously, [Strehl and Ghosh \(2002\)](#) proposed three ensemble clustering methods namely a cluster-based similarity partitioning algorithm, a hyper-graph partitioning algorithm, and a meta-clustering algorithm to combine multiple clustering solutions into one, but the uncertainty in cluster membership was not accounted for. [Fern and Brodley \(2003\)](#) and [Punera and Ghosh \(2008\)](#) extended these approaches, incorporating the posterior probabilities into the ensemble.

Unlike [Russell et al. \(2015\)](#), the proposed ccPGMM takes a divide-and-conquer approach. In ccPGMM, a constrained-PGMM is fitted to M subsets (indexed by m) of $d < p$ randomly selected variables from the high dimensional NIR spectrum. The M posterior probabilities which account for

the uncertainty of the cluster memberships of the N pixels are then consolidated to provide the final consensus clustering solution as follows. An $N \times N$ similarity matrix \mathbf{S}^m for $m = 1, \dots, M$ is computed based on the estimated posterior probabilities $\hat{\mathbf{Z}}^m$ available on convergence of the AEEM after fitting the constrained-PGMM to the subset m . Each entry of \mathbf{S}^m is a similarity score S_{ij}^m computed as

$$S_{ij}^m = \begin{cases} \hat{\mathbf{z}}_i^m (\hat{\mathbf{z}}_j^m)^\top & \text{if } i \neq j, \\ 1 & \text{if } i = j, \end{cases}$$

where $\hat{\mathbf{z}}_i^m$ and $\hat{\mathbf{z}}_j^m$ are the posterior probabilities of cluster membership for observations i and j respectively. The M similarity matrices are then averaged to compute the final similarity matrix \mathbf{S} , whose entries S_{ij} are given by

$$S_{ij} = \frac{1}{M} \sum_{m=1}^M \sum_{g=1}^G \hat{z}_{ig}^m \hat{z}_{jg}^m,$$

where \hat{z}_{ig}^m and \hat{z}_{jg}^m are the posterior probabilities of observation i and j belonging to group g , inferred from data subset m . A dissimilarity matrix \mathbf{D} is then computed as $\mathbf{D} = \mathbf{1} - \mathbf{S}$ and hierarchical clustering with complete linkage (Sokal, 1963) is performed employing \mathbf{D} . As the number of clusters G is known based on the application at hand, the resulting dendrogram is cut to give G clusters and the final consensus clustering solution.

3.4 Technical details

In the proposed ccPGMM, a single constrained-PGMM with a fixed number of clusters G and a fixed number of factors q is fitted to M data subsets with d variables per subset; the values of G , q , M , and d require specification. The number of clusters G is known and fixed in advance according to the particular application. For example, in the motivating application here (see Section 2) where there are three cereal types and the background, $G = 4$. The selection of the number of factors q is based on monitoring the proportion of variance explained by the first q principal components obtained from the application of principal component analysis (PCA) to the entire dataset. There is a trade-off between the values of M , the number of subsets of variables, and d , the number of variables per subset. Typically, d is smaller than p but too small values may provide little clustering information. Further, very large values of d hamper the computational feasibility. Also, the choice of M must be cognisant of the choice of d to ensure good coverage of all the variables in the M data subsets. These choices are explored further in sections 4 and 5.

In terms of specifying the constraints, there are technically no limits on the number of pixels that can be used. The size of the blocks of pixels (constraints) highlighted in Figure 2 can vary and the number of pixels in one block need not be the same as the number of pixels in the other blocks. Usually, the hyperspectral images of food samples are plotted as greyscale images, and the maximum region of pixels that are distinguishable as the background and as the relevant sample under study are selected as constraints. Increasing the number of positive constraints and the number of pixels within the positive constraints does not significantly increase the computational cost of fitting the ccPGMM, as in Melnykov et al. (2016). However, an increase in the number of negative constraints will result in more complex posterior probability calculations in (3), negatively impacting the computational cost. Investigations on the choice of constrained pixels are in sections 4 and 5.

The AEEM algorithm, used to fit the constrained-PGMM to each data subset, is initialized with the cluster labels obtained from applying k -means clustering on the respective data subset. The initial values of $\mathbf{\Lambda}_g$ and $\mathbf{\Psi}_g$ are computed based on the eigenvalue decomposition of $\mathbf{\Sigma}_g$ (McNicholas and Murphy, 2008). The relative change in the log-likelihood is used to assess the convergence of the AEEM with a tolerance of $1e - 6$.

4 Simulation studies

Simulation studies are conducted to assess the performance of ccPGMM and compare it to the performance of the threshold approach and existing state-of-the-art methods such as DBSCAN (Khan et al., 2014; Hahsler et al., 2019), Gaussian mixture models (GMM, Scrucca et al., 2016; McNicholas, 2016;

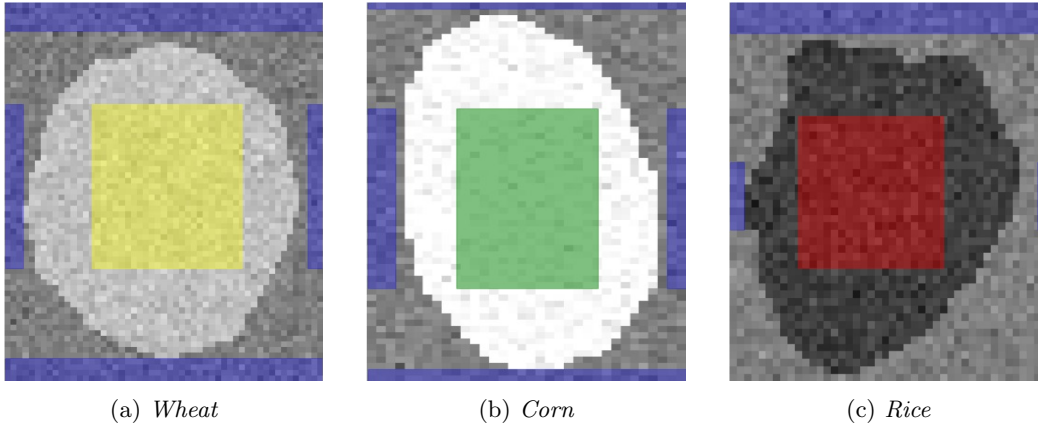


Figure 3: Greyscale image of three simulated hyperspectral images for one of the five well-separated cluster datasets. The pixels in the blue blocks are background, the pixels in the yellow block are wheat, the pixels in the green block are corn and the pixels in the red block are rice.

Bouveyron et al., 2019), PGMM (McNicholas and Murphy, 2008) and consensus PGMM (cPGMM) i.e., ccPGMM with no constraints. The convergence of each model-based clustering approach is assessed with the default parameter settings detailed in the respective R packages. Four scenarios are considered: well-separated clusters (scenario 1), heavily overlapping clusters (scenario 2), mildly overlapping clusters (scenario 3), and synthetic puffed cereal data (scenario 4). For each scenario, five datasets are simulated.

In scenarios 1–3, each simulated dataset contains three simulated hyperspectral images (one for each cereal type), giving a total of $N = 7825$ pixels, where each pixel has an associated $p = 101$ spectrum of strongly correlated variables. The three images are simulated according to labels resulting from applying the threshold approach to three of the hyperspectral images in the motivating dataset detailed in Section 2. The p variables for each of the three types of cereal and the background pixels are generated from different factor analysis models with $q = 3$ and parameters μ_g , Λ_g , and Ψ_g for $g = 1, \dots, G = 4$. To emulate the real data, a strong correlation is induced between the p variables at each pixel by, for every set of 5 consecutive variables, generating the associated values in the loadings matrix from a $\mathcal{N}_q(\mathcal{U}(0.3, 0.9), 0.03)$ and the values of $\text{diag}(\Psi_g)$ from a $\Gamma(\mathcal{U}(0, 0.1), 1)$. The values of the means μ_g for $g = 1, \dots, G$ are used to control the degree of overlap of the clusters in each scenario; details are given in the respective subsections of Section 4. To determine the constraints, the greyscale images of the simulated hyperspectral images are examined to decide on the sets of pixels to be used as constraints, as shown in Figure 3. Here, this resulted in 2,956 pixels of the $N = 7825$ pixels (37.7%) being used to inform the constraints. The 1,356 pixels in the blue blocks (background) must be clustered together, as must the 750 pixels in the yellow block (wheat), the 450 pixels in the green block (corn), and the 400 pixels in the red block (rice). These are the positive constraints. The pixels in one coloured block must not be clustered together with the pixels in another coloured block; these are the negative constraints.

In scenario 4, a synthetic cereal dataset is considered which mirrors the properties of the motivating hyperspectral images. Each dataset contains $L = 9$ simulated hyperspectral images (three for each cereal type) with $N = 28,039$ and where each pixel has an associated $p = 101$ length spectrum. The p variables for each cereal type and background pixels are generated from the relevant factor analyzer model, fitted to the real data; details are discussed in Section 4.4. In this scenario, 12,215 pixels of the $N = 28,039$ pixels (43.5%) are selected as constraints by plotting the greyscale images of the synthetic puffed cereals. Of the 12,215 pixels selected as constraints, 5,900 are background, 3,130 are wheat, 1,535 are corn, and 1,650 are rice. Further, to assess the impact of the proportion of pixels used as constraints on the clustering performance, a smaller set of 6,951 pixels (24.7%) are selected as constraints. Of the 6,951 pixels, 3,801 are background, 1,540 are wheat, 783 are corn and 827 are rice. The set of the 43.5% of pixels and the 24.7% of pixels used as constraints are illustrated in Figures 13 and 14 respectively in Appendix 10.

The simulation study is conducted on an Intel(R) core(TM) i7-10850H CPU @ 2.7 GHz processor with 16 GB RAM and 64-bit operating system. The code used to generate the datasets for each

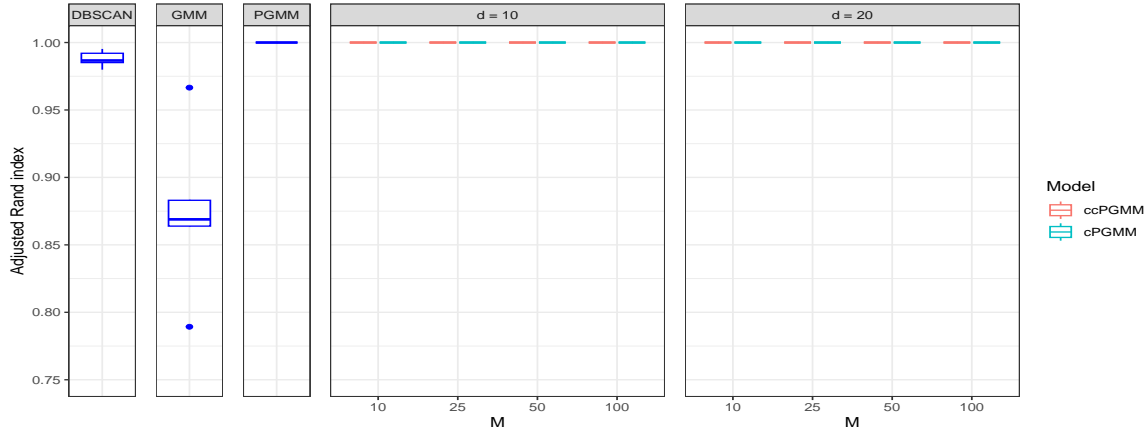


Figure 4: For each of the five simulated datasets with well-separated clusters, the ARI between the known labels and the clustering solutions of DBSCAN, GMM, and PGMM fitted on $p = 101$ variables (first three panels from the left) and cPGMM and ccPGMM (last two panels on the right) fitted with different settings of M and d .

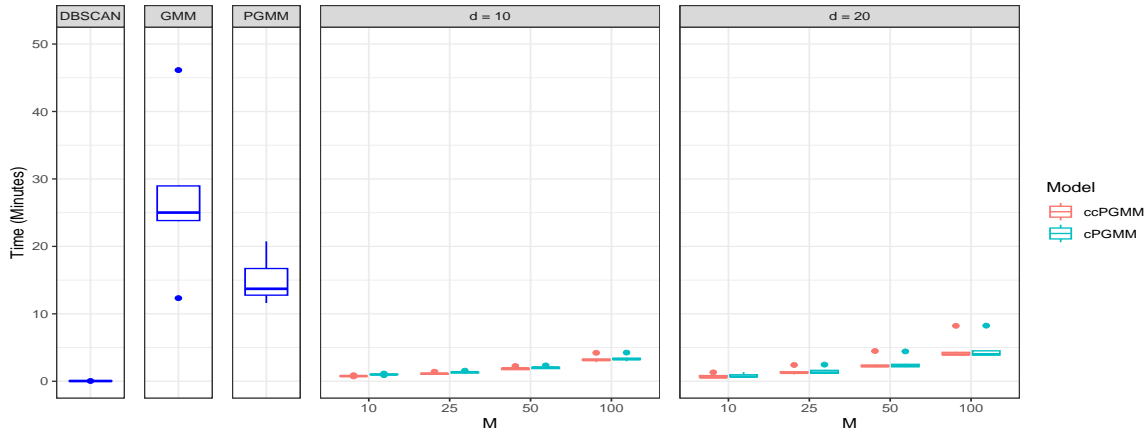


Figure 5: For each of the five simulated datasets with well-separated clusters, the time taken to fit DBSCAN, GMM, and PGMM on $p = 101$ variables (first three panels from the left) and cPGMM and ccPGMM (last two panels on the right) fitted with different settings of M and d .

scenario and to conduct the simulation studies is available on [GitHub](#).

4.1 Scenario 1: well-separated clusters

To generate the well-separated clusters, for $g = 1, \dots, 4$, the cluster mean parameters are generated as $\mu_g \sim \mathcal{N}_p(a, 0.5)$, where $a \in \{0, 5, 10, -5\}$; the p variables of the background, wheat, corn, and rice pixels in each dataset are generated from the four well-separated factor analyzer models, respectively. For DBSCAN, the minimum points required in the neighborhood for core points are set to $2p$, and for the GMM, $G = 4$ is determined by the setting. For the PGMM approaches, $G = 4$ and $q = 1$, where q is informed by fitting PCA to the entire dataset and monitoring the proportion of variance explained by the components. For consensus based approaches, $M = \{10, 25, 50, 100\}$ randomly selected subsets of variables are considered with the number of variables per subset $d = \{10, 20\}$. The positive and negative constraints for ccPGMM are selected as shown in Figure 3.

Figure 4 shows the adjusted Rand index (ARI, [Hubert and Arabie, 1985](#)) between the known labels and the clustering solutions for the five simulated datasets in scenario 1 under the DBSCAN, GMM, PGMM, cPGMM, and ccPGMM approaches. Figure 5 shows the time taken in minutes to fit the methods. All approaches demonstrate strong clustering performance. In terms of computational cost,

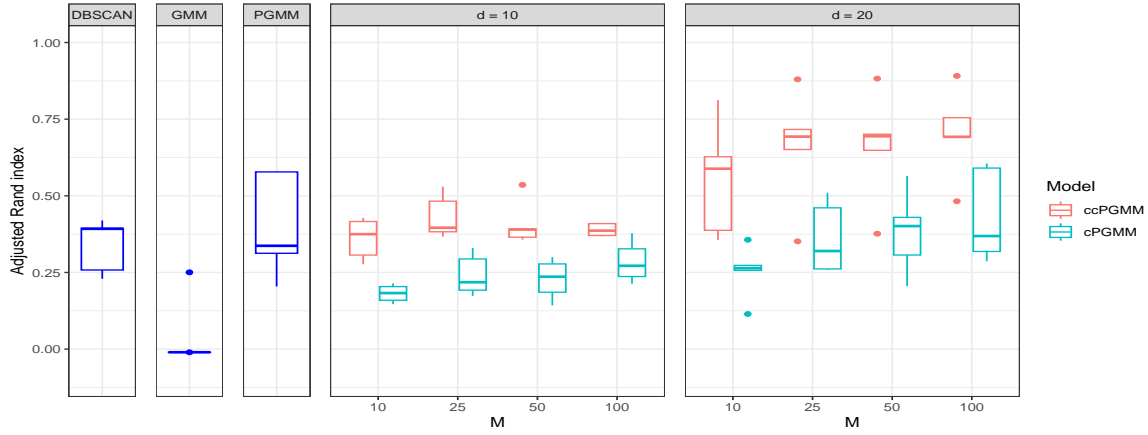


Figure 6: For each of the five datasets with heavily overlapping clusters, the ARI of DBSCAN, GMM, and PGMM fitted on $p = 101$ variables (first three panels from the left) and cPGMM and ccPGMM (last two panels on the right) with different settings of M and d .

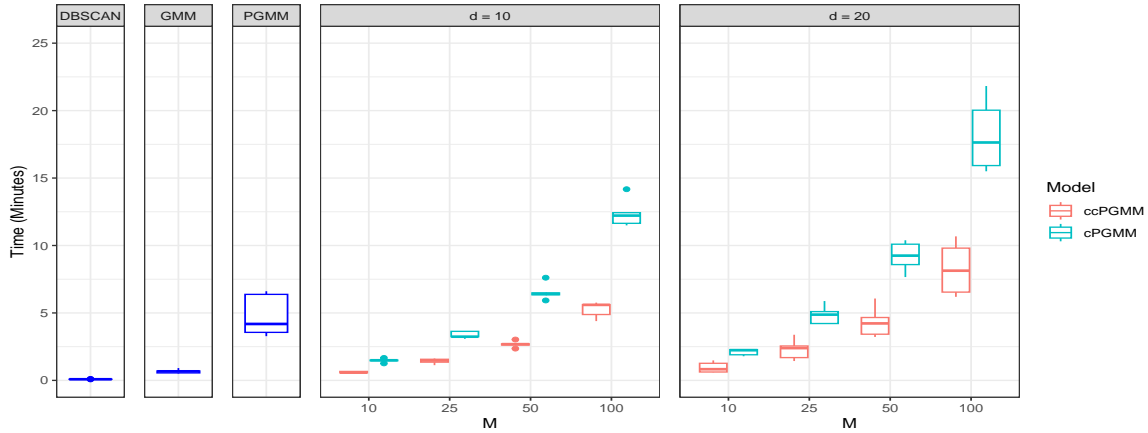


Figure 7: For each of the five datasets with heavily overlapping clusters, the time taken to fit DBSCAN, GMM, and PGMM on $p = 101$ variables (first three panels from the left) and cPGMM and ccPGMM (last two panels on the right) with different settings of M and d .

DBSCAN clusters each dataset in less than a minute while GMM and PGMM take an average of 27 minutes and 15 minutes respectively. The cPGMM and ccPGMM fitted with different settings of M and d have lower computational costs than GMM and PGMM, but similar to DBSCAN, with no loss of accuracy.

4.2 Scenario 2: heavily overlapping clusters

To generate data with heavily overlapping clusters, the cluster mean parameters are generated as $\mu_g \sim \mathcal{N}_p(a, 1.5)$, where $a \in \{1, 1.5, 3, -1.5\}$ for $g = 1, \dots, 4$ respectively. Figures 6 and 7 show the ARI between the known pixel labels and the clustering solutions of DBSCAN, GMM, PGMM, cPGMM, and ccPGMM and the time taken in minutes by each method, respectively. DBSCAN clusters the datasets with an average ARI of 0.34 in less than a minute on average. The GMM struggles to uncover the clustering structure. The PGMM approach performs competitively, achieving an average ARI of 0.40 in 5 minutes on average. The ccPGMM approach performs well in this scenario: with $M \geq 25$ and $d = 20$ an average ARI of 0.66 is achieved, which outperforms PGMM fitted to all p variables. In terms of clustering performance, ccPGMM performs better than cPGMM across all settings of M and d , in comparable time.

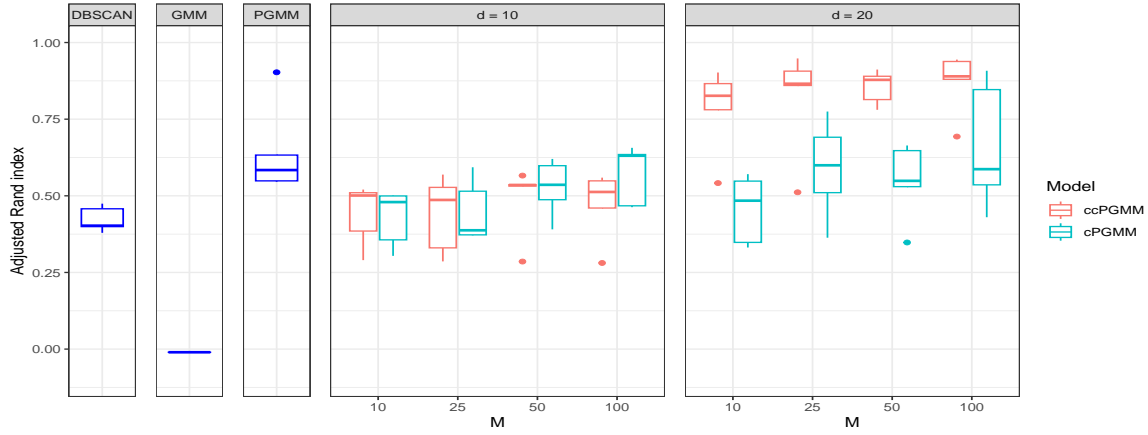


Figure 8: For each of the five datasets with mildly overlapping clusters, the ARI of DBSCAN, GMM, and PGMM fitted on $p = 101$ variables (first three panels from the left) and cPGMM and ccPGMM (last two panels on the right) fitted with different settings of M and d .

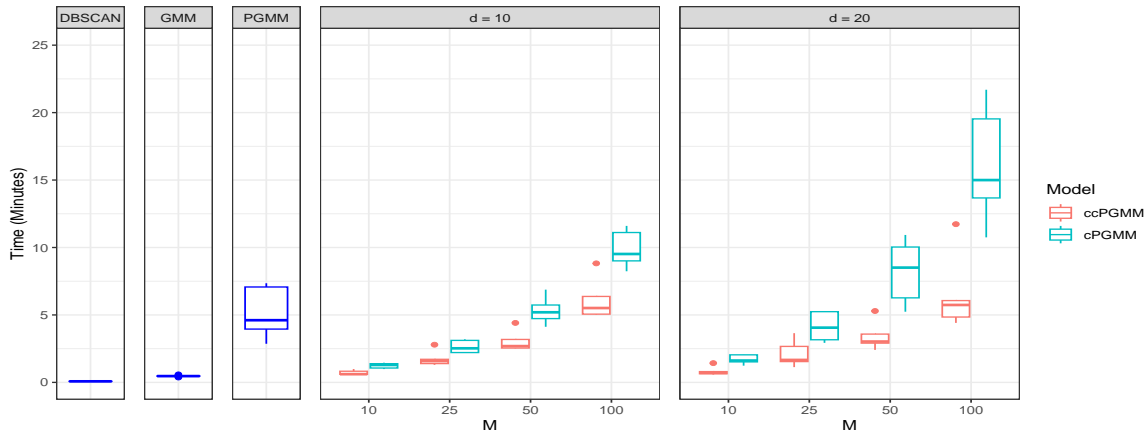


Figure 9: For each of the five datasets with mildly overlapping clusters, the time taken to fit DBSCAN, GMM, and PGMM on $p = 101$ variables (first three panels from the left) and cPGMM and ccPGMM (last two panels on the right) fitted with different settings of M and d .

4.3 Scenario 3: mildly overlapping clusters

The p variables of the background, wheat, corn, and rice pixels in each dataset are generated from four mildly overlapping factor analyzer models, with the cluster mean parameters generated as $\mu_g \sim \mathcal{N}(a, 1.5)$ where $a = \{0, 2, 5, -2\}$ for $g = 1, \dots, 4$, respectively. Figures 8 and 9 show the ARI of the cluster solutions of DBSCAN, GMM, PGMM, cPGMM, and ccPGMM fitted on the five datasets with mildly overlapping clusters and the time taken in minutes to fit them. While GMM again struggles to uncover the clustering structure, DBSCAN and PGMM fitted to all p variables clustered the pixels with an average ARI of 0.42 and 0.64 respectively. In terms of cPGMM and ccPGMM, Figure 8 shows that increasing d from 10 to 20 significantly improves the clustering performance of both methods, with the performance of ccPGMM being the best among the approaches considered. Run times are comparable overall, with cPGMM with the highest values of M and d intuitively taking the longest. The ccPGMM approach with $M \geq 10$ and $d = 20$ is competitively computationally efficient with an average ARI > 0.80 , which has again a much better performance than PGMM fitted to all p variables.

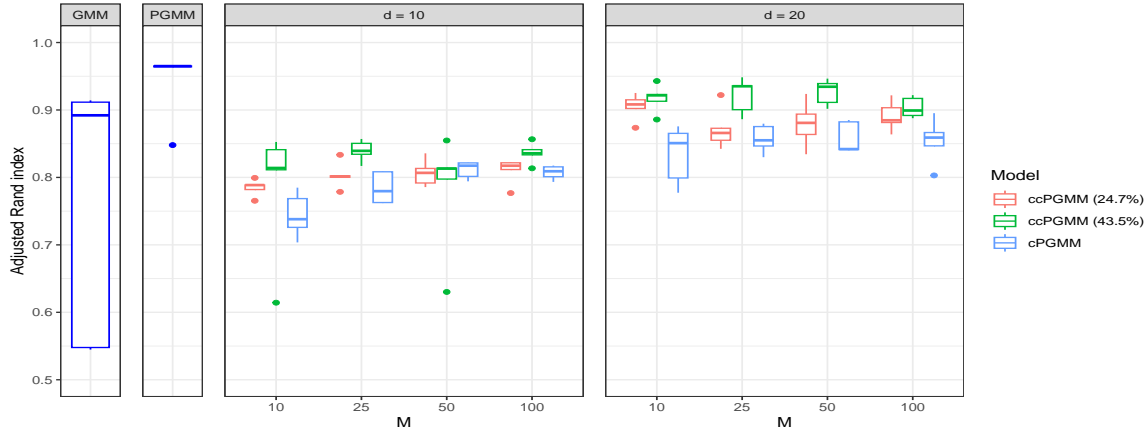


Figure 10: For each of the five synthetic cereal datasets, the ARI of GMM, and PGMM fitted on $p = 101$ variables (first two panels from the left) and cPGMM and ccPGMM (last two panels on the right) fitted with different settings of M and d . For ccPGMM, two settings with 24.7% and 43.5% of pixels used as constraints are shown.

4.4 Scenario 4: synthetic puffed cereal data

Here a synthetic cereal dataset is considered which mirrors the properties of the motivating hyperspectral images. To generate the data, PCA is fitted to the real puffed cereal images and, based on the cumulative proportion of variance explained (Table 2 in Appendix 11), $q = 2$ is selected. Threshold labels, generated as proposed by Xu et al. (2020), are used to identify the pixels belonging to the 3 cereal types and the background in the real puffed cereal images. Four individual factor analysis models with $q = 2$ are then fitted to pixels in the motivating dataset from each label type. Finally, to generate the synthetic cereal images, for each pixel, p variables are generated from the resulting factor analysis models fitted to the background, wheat, corn, and rice pixels in real data.

Figures 10 and 11 show, respectively, the ARI of the cluster solutions of the different clustering methods fitted to the five synthetic cereal datasets, and the time taken in minutes for estimation. Intuitively, since the synthetic cereal datasets are generated from a mixture of factor analyzers, PGMM fitted to all p variables shows strong clustering performance (average ARI of 0.94), however, it takes an average of 50 hours to cluster each synthetic cereal dataset. The GMM approach has a much lower computational cost than PGMM but the quality of the clustering solutions is inconsistent. For DBSCAN (not illustrated), while computationally cheap, clustering performance is poor with an average ARI of 0.32 with a variance of 0.11. The ccPGMM with 43.5% of pixels as constraints and ccPGMM with 24.7% of pixels as constraints fitted with $M \geq 10$ and $d = 20$ shows strong clustering performances. Intuitively, ccPGMM with larger set of constraints (43.5%) performs slightly better than ccPGMM with smaller set of constraints (24.7%) and cPGMM across different settings of M and d . For the ccPGMM approach with 43.5% pixels as constraints, fitted with $M \geq 25$ and $d = 20$ has an average ARI of 0.92. Overall, ccPGMM shows comparable clustering performance to PGMM fitted to all p variables, in less than one-tenth of the computational time.

5 Application to hyperspectral images of puffed cereals

To simultaneously cluster the pixels of the 9 hyperspectral images in the motivating dataset, we apply ccPGMM with $G = 4$, as there are 3 puffed cereal types (wheat, corn, and rice) and the background, and $q = 2$ based on Table 2 in Appendix 11. On the basis of the performance observed in simulation study scenario 4 (Section 4.4) which mirrored the real data, $M = 25$ subsets and $d = 20$ variables per subset were employed. As detailed in Section 4, the greyscale version of the hyperspectral images were considered and, based on pixels for which the labelling was clear, 12, 215 or (43.5%) of the $N = 28, 039$ pixels were selected; these pixels informed the constraints. Also, a smaller set of 6, 951 pixels out of the $N = 28, 039$ pixels (24.7%) are selected as constraints to assess the impact of the proportion of pixels used as constraints on the clustering performance. For comparison purposes, DBSCAN, GMM

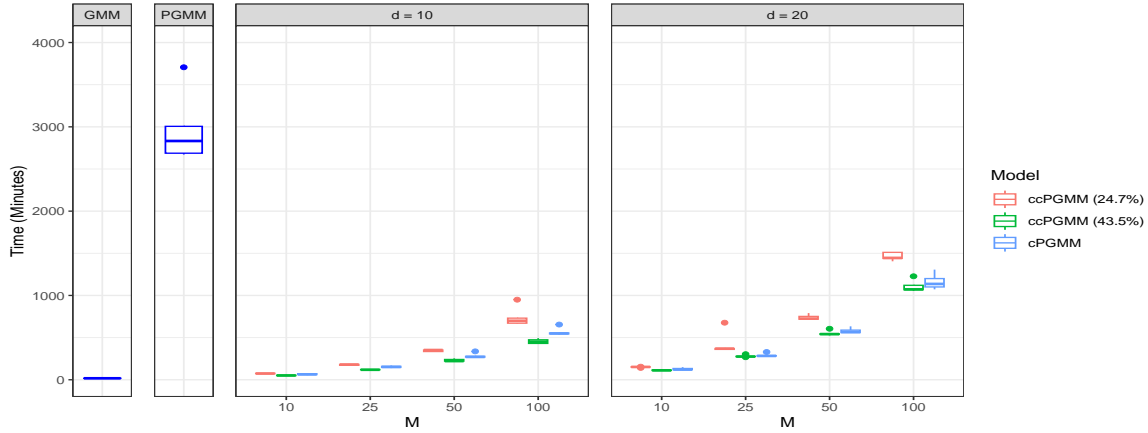


Figure 11: For each of the five synthetic cereal datasets, the time taken to fit GMM, and PGMM on $p = 101$ variables (first two panels from the left) and cPGMM and ccPGMM (last two panels on the right) fitted with different settings of M and d . For ccPGMM, two settings with 24.7% and 43.5% of pixels used as constraints are shown.

with $G = 4$, and PGMM with $G = 4$ and $q = 2$ are fitted to the motivating dataset with all p variables. The threshold approach of Xu et al. (2020) is also applied, individually, to each hyperspectral image to label the pixels.

Figure 12 shows the greyscale images for three of the nine hyperspectral images, and the pixel labels as generated using the threshold approach, DBSCAN, GMM, PGMM, ccPGMM with 43.5% pixels as constraints and ccPGMM with 24.7% pixels as constraints; Figures 15 and 16 in Appendix 12 illustrate the same for the remaining six hyperspectral images. Figures 12d, 12e and 12f show the labels generated for each hyperspectral image by the threshold approach. Each type of pixel is coloured in a different shade of blue according to its label; the resulting labels are very close to the respective greyscale images (12a, 12b, and 12c). However, the threshold approach is ad-hoc involving subjective choice, and does not provide any clustering uncertainties. Figures 12g, 12h and 12i show the cluster solutions of DBSCAN where each pixel is coloured in a different shade of green depending on its label. While DBSCAN correctly distinguishes the background pixels from the cereal pixels in each hyperspectral image, the pixels of the three different cereals are incorrectly allocated to the same cluster. Similarly, GMM clusters the pixels of the three types of cereals into a single cluster as shown in Figures 12j, 12k, and 12l. In addition, GMM allocates the uncertain edge pixels of the cereal grains to a separate cluster and allocates some pixels that likely correspond to spectral noise into another separate cluster. Figures 12m, 12n, and 12o illustrate the pixel labels based on the application of PGMM to all p variables. Each label obtained from the fitted PGMM is coloured in a different shade of purple. Though PGMM has correctly allocated several background and cereal pixels to their respective separate clusters, it also appears to have incorrectly clustered some together, giving non-contiguous images. In Figure 12n, which shows a corn cereal, many background pixels are allocated to the corn cluster. In Figure 12m and 12o, corresponding to wheat and rice cereals respectively, several edge pixels of the cereals are incorrectly allocated to the corn cluster. In addition, PGMM takes nearly 72 hours to cluster the motivating dataset.

Finally, Figures 12p, 12q and 12r show the labels of the pixels, in different shades of brown, obtained by applying ccPGMM with 43.5% of pixels as constraints. Applying ccPGMM to all nine hyperspectral images simultaneously took only 6 hours and the cluster labels are close to labels obtained by applying the threshold approach to each image individually. Compared to the other clustering solutions considered, ccPGMM distinguishes the cereals well from the background while, overall, pixels are allocated to different clusters corresponding to corn, wheat, and rice. However, some pixels are still incorrectly mixed across clusters, particularly around the edges of the wheat and rice cereals. Figures 12s, 12t and 12u show the cluster labels obtained by applying ccPGMM with 24.7% pixels as constraints in different shades of brown. The ccPGMM fitted with 24.7% of pixels as constraints cluster the pixels as well as the ccPGMM with 43.5% of pixels as constraints. However, some pixels around the edges of the wheat and corn cereal are incorrectly clustered as rice. Importantly, the uncertainties

associated with the cluster membership for each pixel are available given the model-based approach to clustering and the uncertainty plots are given in Figures 17, 18, and 19 in Appendix 13; intuitively the pixels around the edges of the cereals have the highest clustering uncertainties.

6 Discussion

A novel model-based approach to simultaneously labelling pixels of hyperspectral images while availing of additional information about the relationship between groups of pixels within the images is proposed. The proposed ccPGMM demonstrates strong clustering performance when compared to existing approaches both in terms of quality of the clustering solution, and the computational time required to cluster such a large dataset.

While the ccPGMM approach is less subjective than the currently used threshold approach, user decisions must still be made. For example, the selection of the number of factors q , while well established, is subjective. Examining alternative approaches to choosing q either using model selection criteria or using shrinkage priors (Bhattacharya and Dunson, 2011) in a Bayesian context would address this, but increase the computational cost. Indeed, under the ccPGMM approach, allowing for different values of q when fitting to the M different subsets of variables could bring improved performance but would require further exploration. Further, the choice of M and d are currently data-driven and therefore subjective. Additionally, similar to Jacques and Ruckebusch (2016), considering co-clustering in the context of ccPGMM would facilitate both clustering of pixels and wavelengths.

Overall, the proposed ccPGMM model works well when clustering a large number of pixels in a set of hyperspectral images, and provides associated clustering uncertainty, in a computationally efficient manner. As such, the approach should have a broader application to other hyperspectral images where labelling of the pixels is required.

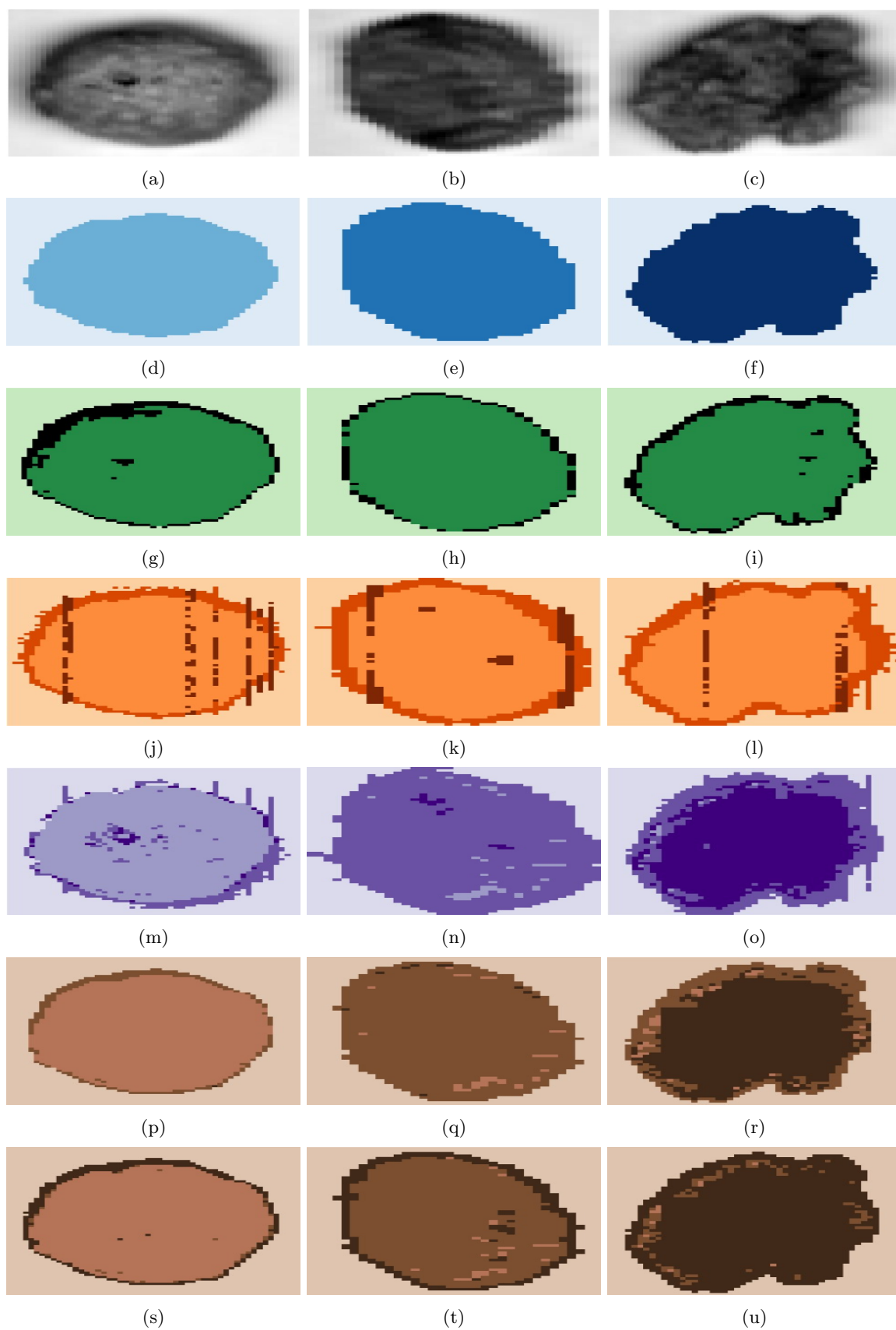


Figure 12: *Greyscale images and pixel labels for three of the nine hyperspectral images ($l = \{1, 4, 7\}$) of the cereals using the threshold approach, DBSCAN, MBC, PGMM, ccPGMM with 43.5% of pixels as constraints, and ccPGMM with 24.7% of pixels as constraints respectively for wheat (12a, 12d, 12g, 12j, 12m, 12p, 12s), corn (12b, 12e, 12h, 12k, 12n, 12q, 12t) and rice (12c, 12f, 12i, 12l, 12o, 12r, 12u).*

7 Acknowledgement

This publication has emanated from research conducted with the financial support of Science Foundation Ireland under Grant number 18/CRT/6049. For the purpose of Open Access, the author has applied a CC BY public copyright licence to any Author Accepted Manuscript version arising from this submission.

References

- Abdi, H. and Williams, L. J. (2010). Principal component analysis. *Wiley interdisciplinary reviews: computational statistics*, 2(4):433–459.
- Amigo, J. M. (2010). Practical issues of hyperspectral imaging analysis of solid dosage forms. *Analytical and bioanalytical chemistry*, 398(1):93–109.
- Amigo, J. M. (2020). Hyperspectral and multispectral imaging: Setting the scene. In *Data Handling in Science and Technology*, volume 32, pages 3–16. Elsevier.
- Amigo, J. M., Babamoradi, H., and Elcoroaristizabal, S. (2015). Hyperspectral image analysis. a tutorial. *Analytica chimica acta*, 896:34–51.
- Amigo, J. M. and Santos, C. (2020). Preprocessing of hyperspectral and multispectral images. In *Data handling in science and technology*, volume 32, pages 37–53. Elsevier.
- Bhattacharya, A. and Dunson, D. B. (2011). Sparse Bayesian infinite factor models. *Biometrika*, 98(2):291–306.
- Bocklitz, T., Walter, A., Hartmann, K., Rösch, P., and Popp, J. (2011). How to pre-process Raman spectra for reliable and stable models? *Analytica chimica acta*, 704(1-2):47–56.
- Bouveyron, C. and Brunet-Saumard, C. (2014). Discriminative variable selection for clustering with the sparse fisher-em algorithm. *Computational Statistics*, 29(3):489–513.
- Bouveyron, C., Celeux, G., Murphy, T. B., and Raftery, A. E. (2019). *Model-based clustering and classification for data science: with applications in R*, volume 50. Cambridge University Press.
- Feng, Y.-Z. and Sun, D.-W. (2012). Application of hyperspectral imaging in food safety inspection and control: a review. *Critical reviews in food science and nutrition*, 52(11):1039–1058.
- Fern, X. Z. and Brodley, C. E. (2003). Random projection for high dimensional data clustering: A cluster ensemble approach. In *Proceedings of the 20th international conference on machine learning (ICML-03)*, pages 186–193.
- Geladi, P., MacDougall, D., and Martens, H. (1985). Linearization and scatter-correction for near-infrared reflectance spectra of meat. *Applied spectroscopy*, 39(3):491–500.
- Ghahramani, Z., Hinton, G. E., et al. (1996). The EM algorithm for mixtures of factor analyzers. Technical report, Technical Report CRG-TR-96-1, University of Toronto.
- Gowen, A. A., Xu, J.-L., and Herrero-Langreo, A. (2019). Comparison of spectral selection methods in the development of classification models from visible near infrared hyperspectral imaging data. *Journal of Spectral Imaging*, 8.
- Hahsler, M., Piekenbrock, M., and Doran, D. (2019). DBscan: Fast density-based clustering with R. *Journal of Statistical Software*, 91:1–30.
- Hubert, L. and Arabie, P. (1985). Comparing partitions. *Journal of classification*, 2:193–218.
- Jacques, J. and Ruckebusch, C. (2016). Model-based co-clustering for hyperspectral images. *Journal of Spectral Imaging*.
- Khan, K., Rehman, S. U., Aziz, K., Fong, S., and Sarasvady, S. (2014). DBscan: Past, present and future. In *The fifth international conference on the applications of digital information and web technologies (ICADIWT 2014)*, pages 232–238. IEEE.
- McLachlan, G. and Peel, D. (2000). Mixtures of factor analyzers. In *In Proceedings of the Seventeenth International Conference on Machine Learning*. Citeseer.

- McLachlan, G. J. and Peel, D. (2004). *Finite mixture models*. John Wiley & Sons.
- McLachlan, G. J., Peel, D., and Bean, R. W. (2003). Modelling high-dimensional data by mixtures of factor analyzers. *Computational Statistics & Data Analysis*, 41(3-4):379–388.
- McNicholas, P. D. (2016). Model-based clustering. *Journal of Classification*, 33(3):331–373.
- McNicholas, P. D. and Murphy, T. B. (2008). Parsimonious Gaussian mixture models. *Statistics and Computing*, 18(3):285–296.
- McNicholas, P. D., Murphy, T. B., McDaid, A. F., and Frost, D. (2010). Serial and parallel implementations of model-based clustering via parsimonious Gaussian mixture models. *Computational Statistics & Data Analysis*, 54(3):711–723.
- Melnykov, V., Melnykov, I., and Michael, S. (2016). Semi-supervised model-based clustering with positive and negative constraints. *Advances in data analysis and classification*, 10(3):327–349.
- Neath, A. A. and Cavanaugh, J. E. (2012). The Bayesian information criterion: background, derivation, and applications. *Wiley Interdisciplinary Reviews: Computational Statistics*, 4(2):199–203.
- Pal, N. R. and Pal, S. K. (1993). A review on image segmentation techniques. *Pattern recognition*, 26(9):1277–1294.
- Punera, K. and Ghosh, J. (2008). Consensus-based ensembles of soft clusterings. *Applied Artificial Intelligence*, 22(7-8):780–810.
- R Core Team (2023). *R: A Language and Environment for Statistical Computing*. R Foundation for Statistical Computing, Vienna, Austria.
- Rinnan, Å., Van Den Berg, F., and Engelsen, S. B. (2009). Review of the most common pre-processing techniques for near-infrared spectra. *TrAC Trends in Analytical Chemistry*, 28(10):1201–1222.
- Russell, N., Murphy, T. B., and Raftery, A. E. (2015). Bayesian model averaging in model-based clustering and density estimation. *arXiv preprint arXiv:1506.09035*.
- Schwarz, G. (1978). Estimating the dimension of a model. *The Annals of Statistics*, 6(2):461–464.
- Scrucca, L., Fop, M., Murphy, T. B., and Raftery, A. E. (2016). mclust 5: clustering, classification and density estimation using Gaussian finite mixture models. *The R Journal*, 8(1):289–317.
- Sokal, R. R. (1963). The principles and practice of numerical taxonomy. *Taxon*, pages 190–199.
- Strehl, A. and Ghosh, J. (2002). Cluster ensembles—a knowledge reuse framework for combining multiple partitions. *Journal of machine learning research*, 3(Dec):583–617.
- Xu, J.-L., Riccioli, C., Herrero-Langreo, A., and Gowen, A. A. (2020). Deep learning classifiers for near infrared spectral imaging: a tutorial. *Journal of Spectral Imaging*, 9.
- Zhai, H., Zhang, H., Li, P., and Zhang, L. (2021). Hyperspectral image clustering: Current achievements and future lines. *IEEE Geoscience and Remote Sensing Magazine*, 9(4):35–67.

8 Appendix A

As discussed in Section 2, Table 1 details the dimensionality of the nine hyperspectral images of the three puffed cereals.

Table 1: *The dimensionality of motivating hyperspectral images of puffed cereals.*

Puffed cereal type	l	S_l	T_l	$S_l \times T_l$
Wheat	1	67	53	3551
Wheat	2	62	64	3968
Wheat	3	65	55	3575
Corn	4	61	34	2074
Corn	5	39	69	2691
Corn	6	56	54	3024
Rice	7	56	49	2744
Rice	8	78	54	4212
Rice	9	50	44	2200

9 Appendix B: AECM for constrained-PGMM

In constrained-PGMM, the observed data log-likelihood is

$$\ell_o(\mathbf{X}) = \sum_{n=1}^N \log \sum_{g=1}^G \tau_g f(\mathbf{x}_n; \boldsymbol{\mu}_g, \boldsymbol{\Lambda}_g, \boldsymbol{\Psi}_g). \quad (4)$$

As (4) is difficult to maximize directly, an AECM algorithm is used to fit the constrained-PGMM. AECM works in two cycles and allows for a different definition of the complete data in each cycle to estimate the parameters.

9.1 First cycle

In the first cycle, the component indicators $\mathbf{Z} = \{\mathbf{z}_1, \dots, \mathbf{z}_N\}$ are assumed to be the missing data, where \mathbf{z}_N is a binary vector of length G . The complete data log-likelihood is

$$\ell_c(\mathbf{X}, \mathbf{Z}) = \sum_{n=1}^N \sum_{g=1}^G z_{ng} [\log \tau_g + \log f(\mathbf{x}_n; \boldsymbol{\mu}_g, \boldsymbol{\Lambda}_g, \boldsymbol{\Psi}_g)], \quad (5)$$

where $f(\mathbf{x}_n; \boldsymbol{\mu}_g, \boldsymbol{\Lambda}_g, \boldsymbol{\Psi}_g) \sim \mathcal{N}_p(\boldsymbol{\mu}_g, \boldsymbol{\Lambda}_g \boldsymbol{\Lambda}_g^\top + \boldsymbol{\Psi}_g)$.

9.1.1 E-step:

The expected complete data log-likelihood is,

$$\begin{aligned} Q_1(\boldsymbol{\mu}_g, \tau_g) = \sum_{n=1}^N \sum_{g=1}^G E[z_{ng}; \mathbf{x}_n] & \left[\log \tau_g - \frac{p}{2} \log(2\pi) \right. \\ & \left. - \frac{1}{2} \log(|\boldsymbol{\Lambda}_g \boldsymbol{\Lambda}_g^\top + \boldsymbol{\Psi}_g|) \right. \\ & \left. - \frac{1}{2} [(\mathbf{x}_n - \boldsymbol{\mu}_g)^\top (\boldsymbol{\Lambda}_g \boldsymbol{\Lambda}_g^\top + \boldsymbol{\Psi}_g)^{-1} (\mathbf{x}_n - \boldsymbol{\mu}_g)] \right]. \end{aligned}$$

The posterior probability \hat{z}_{ng} of observation n belonging to cluster g is

$$\begin{aligned} E[z_{ng} | \mathbf{x}_n] = \hat{z}_{ng} & = \Pr(z_{ng} = 1; \mathbf{x}_n, \hat{\tau}_g, \hat{\boldsymbol{\mu}}_g, \hat{\boldsymbol{\Lambda}}_g, \hat{\boldsymbol{\Psi}}_g), \\ \hat{z}_{ng} & = \frac{\hat{\tau}_g \mathcal{N}_p(\mathbf{x}_n; \hat{\boldsymbol{\mu}}_g, \hat{\boldsymbol{\Lambda}}_g \hat{\boldsymbol{\Lambda}}_g^\top + \hat{\boldsymbol{\Psi}}_g)}{\sum_{g'=1}^G \hat{\tau}_{g'} \mathcal{N}_p(\mathbf{x}_n; \hat{\boldsymbol{\mu}}_{g'}, \hat{\boldsymbol{\Lambda}}_{g'} \hat{\boldsymbol{\Lambda}}_{g'}^\top + \hat{\boldsymbol{\Psi}}_{g'})}. \end{aligned}$$

where $\hat{\cdot}$ denotes an initial or current parameter estimate, as relevant.

Let B_1 be the set of J pixels (indexed by j) in the blue blocks shown in Figure 2 which are known to be background and must be clustered together. This is a positive constraint (denoted by $+$). The posterior probability $\hat{z}_{B_1,g}^+$ of the pixels in B_1 belonging to cluster g given the positive constraints ($+$) is

$$\hat{z}_{B_1,g}^+ = \frac{\prod_{j \in B_1} \hat{\tau}_g \mathcal{N}_p(\mathbf{x}_j; \hat{\boldsymbol{\mu}}_g, \hat{\boldsymbol{\Lambda}}_g \hat{\boldsymbol{\Lambda}}_g^\top + \hat{\boldsymbol{\Psi}}_g)}{\sum_{g'=1}^G \prod_{j \in B_1} \hat{\tau}_{g'} \mathcal{N}_p(\mathbf{x}_j; \hat{\boldsymbol{\mu}}_{g'}, \hat{\boldsymbol{\Lambda}}_{g'} \hat{\boldsymbol{\Lambda}}_{g'}^\top + \hat{\boldsymbol{\Psi}}_{g'})}.$$

Let B_2 be the set of O pixels (indexed by o) in the yellow block of Figure 2 which are known to be wheat and should be clustered together. These are positive constraints (denoted $+$). However, the pixels in B_1 should not be clustered together with the pixels in B_2 . This is a negative constraint (denoted $-$). Let A be the event that pixels in B_1 belong to cluster g and B be the event that pixels in B_2 belong to any cluster f in G but $f \neq g$ and vice versa. Then the probability of event A and B occurring together is

$$\Pr(A \cap B) = \Pr(A) \Pr(B). \quad (6)$$

Based on equation (6), the posterior probability $\hat{z}_{B_1,g}^{\pm}$ of the pixels in B_1 belonging to cluster g , given the positive and negative constraints \pm is

$$\hat{z}_{B_1,g}^+ = \frac{\prod_{j \in B_1} \hat{\tau}_g \mathcal{N}_p(\mathbf{x}_j; \hat{\boldsymbol{\mu}}_g, \hat{\boldsymbol{\Lambda}}_g \hat{\boldsymbol{\Lambda}}_g^\top + \hat{\boldsymbol{\Psi}}_g) \sum_{\substack{f=1 \\ f \neq g}}^G \prod_{\substack{o \in B_2 \\ o=1}}^O \hat{\tau}_f \mathcal{N}_p(\mathbf{x}_o; \hat{\boldsymbol{\mu}}_f, \hat{\boldsymbol{\Lambda}}_f \hat{\boldsymbol{\Lambda}}_f^\top + \hat{\boldsymbol{\Psi}}_f)}{\sum_{g'=1}^G \prod_{j \in B_1} \hat{\tau}_{g'} \mathcal{N}_p(\mathbf{x}_j; \hat{\boldsymbol{\mu}}_{g'}, \hat{\boldsymbol{\Lambda}}_{g'} \hat{\boldsymbol{\Lambda}}_{g'}^\top + \hat{\boldsymbol{\Psi}}_{g'}) \sum_{\substack{f=1 \\ f \neq g'}}^G \prod_{\substack{o \in B_2 \\ o=1}}^O \hat{\tau}_f \mathcal{N}_p(\mathbf{x}_o; \hat{\boldsymbol{\mu}}_f, \hat{\boldsymbol{\Lambda}}_f \hat{\boldsymbol{\Lambda}}_f^\top + \hat{\boldsymbol{\Psi}}_f)}. \quad (7)$$

Similarly, the posterior probability $\hat{z}_{B_2,g}^{\pm}$ of the pixels in B_2 belonging to cluster g , given the positive and negative constraints \pm is

$$\hat{z}_{B_2,g}^+ = \frac{\prod_{\substack{o \in B_2 \\ o=1}}^O \hat{\tau}_g \mathcal{N}_p(\mathbf{x}_o; \hat{\boldsymbol{\mu}}_g, \hat{\boldsymbol{\Lambda}}_g \hat{\boldsymbol{\Lambda}}_g^\top + \hat{\boldsymbol{\Psi}}_g) \sum_{\substack{f=1 \\ f \neq g}}^G \prod_{\substack{j \in B_1 \\ j=1}}^J \hat{\tau}_f \mathcal{N}_p(\mathbf{x}_j; \hat{\boldsymbol{\mu}}_f, \hat{\boldsymbol{\Lambda}}_f \hat{\boldsymbol{\Lambda}}_f^\top + \hat{\boldsymbol{\Psi}}_f)}{\sum_{g'=1}^G \prod_{\substack{o \in B_2 \\ o=1}}^O \hat{\tau}_{g'} \mathcal{N}_p(\mathbf{x}_o; \hat{\boldsymbol{\mu}}_{g'}, \hat{\boldsymbol{\Lambda}}_{g'} \hat{\boldsymbol{\Lambda}}_{g'}^\top + \hat{\boldsymbol{\Psi}}_{g'}) \sum_{\substack{f=1 \\ f \neq g'}}^G \prod_{\substack{j \in B_1 \\ j=1}}^J \hat{\tau}_f \mathcal{N}_p(\mathbf{x}_j; \hat{\boldsymbol{\mu}}_f, \hat{\boldsymbol{\Lambda}}_f \hat{\boldsymbol{\Lambda}}_f^\top + \hat{\boldsymbol{\Psi}}_f)}.$$

The remaining pixels in Figure 2 which are not in the highlighted blocks are considered as blocks with only one pixel and no negative constraints.

9.1.2 CM-step:

The expected complete data log-likelihood can be rewritten as

$$Q_1(\boldsymbol{\mu}_g, \tau_g) = \sum_{n=1}^N \sum_{g=1}^G \hat{z}_{ng}^+ \left[\log \tau_g - \frac{p}{2} \log(2\pi) - \frac{1}{2} \log(|\boldsymbol{\Lambda}_g \boldsymbol{\Lambda}_g^\top + \boldsymbol{\Psi}_g|) - \frac{1}{2} [(\mathbf{x}_n - \boldsymbol{\mu}_g)^\top (\boldsymbol{\Lambda}_g \boldsymbol{\Lambda}_g^\top + \boldsymbol{\Psi}_g)^{-1} (\mathbf{x}_n - \boldsymbol{\mu}_g)] \right]. \quad (8)$$

Differentiating (8) with respect to $\boldsymbol{\mu}_g$,

$$\hat{\boldsymbol{\mu}}_g = \frac{\sum_{n=1}^N \hat{z}_{ng}^+ \mathbf{x}_n}{\sum_{n=1}^N \hat{z}_{ng}^+}.$$

Differentiating (8) with respect to τ_g ,

$$\hat{\tau}_g = \frac{\sum_{n=1}^N \hat{z}_{ng}^+}{N}.$$

9.2 Second cycle

In the second cycle, both component indicators $\mathbf{Z} = \{\mathbf{z}_1, \dots, \mathbf{z}_n\}$ and latent factors $\mathbf{U} = \{\mathbf{u}_1, \dots, \mathbf{u}_n\}$ are assumed to be the missing data. Therefore, the complete data log-likelihood is

$$\ell_c(\mathbf{X}, \mathbf{Z}, \mathbf{U}) = \sum_{n=1}^N \sum_{g=1}^G z_{ng} [\log \tau_g + \log f(\mathbf{x}_n; \boldsymbol{\mu}_g, \boldsymbol{\Lambda}_g, \boldsymbol{\Psi}_g, \mathbf{u}_n) + \log f(\mathbf{u}_n)],$$

where $f(\mathbf{x}_n; \boldsymbol{\mu}_g, \boldsymbol{\Lambda}_g, \boldsymbol{\Psi}_g, \mathbf{u}_n) \sim \mathcal{N}_p(\boldsymbol{\mu}_g + \boldsymbol{\Lambda}_g \mathbf{u}_n, \boldsymbol{\Psi}_g)$ and $f(\mathbf{u}_n) \sim \mathcal{N}_q(0, I)$.

The complete data log-likelihood can be rewritten as,

$$\begin{aligned} \ell_c(\mathbf{X}, \mathbf{Z}, \mathbf{U}) = C + \sum_{g=1}^G \left[\mathbf{n}_g \log \tau_g - \frac{\mathbf{n}_g}{2} \log(|\boldsymbol{\Psi}_g|) - \frac{1}{2} \left[\sum_{n=1}^N z_{ng} [(\mathbf{x}_n - \boldsymbol{\mu}_g)^\top \boldsymbol{\Psi}_g^{-1} (\mathbf{x}_n - \boldsymbol{\mu}_g)] \right. \right. \\ \left. \left. + \sum_{n=1}^N z_{ng} [(\mathbf{x}_n - \boldsymbol{\mu}_g)^\top \boldsymbol{\Psi}_g^{-1} (\boldsymbol{\Lambda}_g \mathbf{u}_n)] \right. \right. \\ \left. \left. - \frac{1}{2} (\boldsymbol{\Lambda}_g^\top \boldsymbol{\Psi}_g^{-1} \boldsymbol{\Lambda}_g \sum_{n=1}^N z_{ng} \mathbf{u}_n \mathbf{u}_n^\top)^\top \right], \end{aligned}$$

where C is the constant and $\mathbf{n}_g = \sum_{n=1}^N z_{ng}$.

9.2.1 E-step:

The expected complete data log-likelihood is,

$$\begin{aligned} Q_2(\boldsymbol{\Lambda}_g, \boldsymbol{\Psi}_g) = C + \sum_{g=1}^G \left[\mathbf{n}_g \log \tau_g - \frac{\mathbf{n}_g}{2} \log(|\boldsymbol{\Psi}_g|) - \frac{\mathbf{n}_g}{2} (\boldsymbol{\Psi}_g^{-1} \mathbf{S}_g)^\top \right. \\ \left. + \sum_{n=1}^N E[z_{ng}; \mathbf{x}_n] [(\mathbf{x}_n - \boldsymbol{\mu}_g)^\top \boldsymbol{\Psi}_g^{-1} (\boldsymbol{\Lambda}_g E[\mathbf{u}_n; \mathbf{x}_n])] \right. \\ \left. - \frac{1}{2} (\boldsymbol{\Lambda}_g^\top \boldsymbol{\Psi}_g^{-1} \boldsymbol{\Lambda}_g \sum_{n=1}^N E[z_{ng}; \mathbf{x}_n] E[\mathbf{u}_n \mathbf{u}_n^\top; \mathbf{x}_n])^\top \right], \end{aligned} \quad (9)$$

where $\mathbf{S}_g = \frac{1}{\mathbf{n}_g} \sum_{n=1}^N z_{ng} (\mathbf{x}_n - \boldsymbol{\mu}_g) (\mathbf{x}_n - \boldsymbol{\mu}_g)^\top$.

The expected value $E[z_{ng} | \mathbf{x}_n] = \hat{z}_{ng}$ is computed with $\boldsymbol{\mu}_g = \hat{\boldsymbol{\mu}}_g$ and $\tau_g = \hat{\tau}_g$ updated in the CM-step of the first cycle with the known positive and negative constraints. The posterior probability $\hat{z}_{B_1, g}^+$ of the pixels in B_1 belonging to cluster g , given the positive and negative constraints \pm is

$$\hat{z}_{B_1, g}^+ = \frac{\prod_{j \in B_1} \hat{\tau}_g \mathcal{N}_p(\mathbf{x}_j; \hat{\boldsymbol{\mu}}_g, \hat{\boldsymbol{\Lambda}}_g \hat{\boldsymbol{\Lambda}}_g^\top + \hat{\boldsymbol{\Psi}}_g) \sum_{f=1, f \neq g}^G \prod_{o \in B_2} \hat{\tau}_f \mathcal{N}_p(\mathbf{x}_o; \hat{\boldsymbol{\mu}}_f, \hat{\boldsymbol{\Lambda}}_f \hat{\boldsymbol{\Lambda}}_f^\top + \hat{\boldsymbol{\Psi}}_f)}{\sum_{g'=1}^G \prod_{j \in B_1} \hat{\tau}_{g'} \mathcal{N}_p(\mathbf{x}_j; \hat{\boldsymbol{\mu}}_{g'}, \hat{\boldsymbol{\Lambda}}_{g'} \hat{\boldsymbol{\Lambda}}_{g'}^\top + \hat{\boldsymbol{\Psi}}_{g'}) \sum_{f=1, f \neq g'}^G \prod_{o \in B_2} \hat{\tau}_f \mathcal{N}_p(\mathbf{x}_o; \hat{\boldsymbol{\mu}}_f, \hat{\boldsymbol{\Lambda}}_f \hat{\boldsymbol{\Lambda}}_f^\top + \hat{\boldsymbol{\Psi}}_f)}. \quad (10)$$

Similarly, the computation is repeated for estimating the posterior probabilities of pixels in B_2 belonging to cluster g with pixels in B_1 as negative constraints. The expected value $E[\mathbf{u}_n | \mathbf{x}_n]$ is computed by considering a joint Gaussian distribution between \mathbf{x}_n and \mathbf{u}_n . By Gaussian conditioning formulas,

$$E[\mathbf{u}_n | \mathbf{x}_n] = \hat{\Lambda}_g^\top (\hat{\Lambda}_g \hat{\Lambda}_g^\top + \hat{\Psi}_g)^{-1} (\mathbf{x}_n - \hat{\mu}_g).$$

Also,

$$E[\mathbf{u}_n \mathbf{u}_n^\top | \mathbf{x}_n] = \mathbf{I}_q - \hat{\beta}_g \hat{\Lambda}_g + \hat{\beta}_g (\mathbf{x}_n - \hat{\mu}_g) (\mathbf{x}_n - \hat{\mu}_g)^\top \hat{\beta}_g^\top,$$

where $\hat{\beta}_g = \hat{\Lambda}_g^\top (\hat{\Lambda}_g \hat{\Lambda}_g^\top + \hat{\Psi}_g)^{-1}$.

9.2.2 CM-step:

The expected complete log-likelihood can be rewritten as

$$Q_2(\Lambda_g, \Psi_g) = C + \sum_{g=1}^G \mathbf{n}_g \left[-\frac{1}{2} \log |\Psi_g| - \frac{1}{2} [\Psi_g^{-1} \mathbf{S}_g]^\top + [\Psi_g^{-1} \Lambda_g \hat{\beta}_g \mathbf{S}_g]^\top - \frac{1}{2} [\Lambda_g^\top \Psi_g^{-1} \Lambda_g \Theta_g] \right], \quad (11)$$

where,

$$\begin{aligned} \Theta_g &= \mathbf{I}_q - \hat{\beta}_g \Lambda_g + \hat{\beta}_g \mathbf{S}_g \hat{\beta}_g^\top, \\ \mathbf{S}_g &= \frac{1}{\mathbf{n}_g} \sum_{n=1}^N \hat{z}_{ng}^+ (\mathbf{x}_n - \hat{\mu}_g) (\mathbf{x}_n - \hat{\mu}_g)^\top, \\ \mathbf{n}_g &= \sum_{n=1}^N \hat{z}_{ng}^+. \end{aligned}$$

Differentiating 11 with respect to Λ_g

$$\hat{\Lambda}_g = \mathbf{S}_g \hat{\beta}_g^\top \Theta_g^{-1}.$$

Differentiating 11 with respect to Ψ_g^{-1}

$$\hat{\Psi}_g = \text{diag}[\mathbf{S}_g - \hat{\Lambda}_g \hat{\beta}_g \mathbf{S}_g].$$

The algorithm iteratively updates the parameters until convergence and the posterior probabilities z_{ng} at convergence are used to compute the similarity matrix in the consensus approach.

10 Appendix C

As discussed in Section 4, Figures 13 and 14 highlight the 43.5% of pixels and 24.7% of pixels used as constraints respectively.

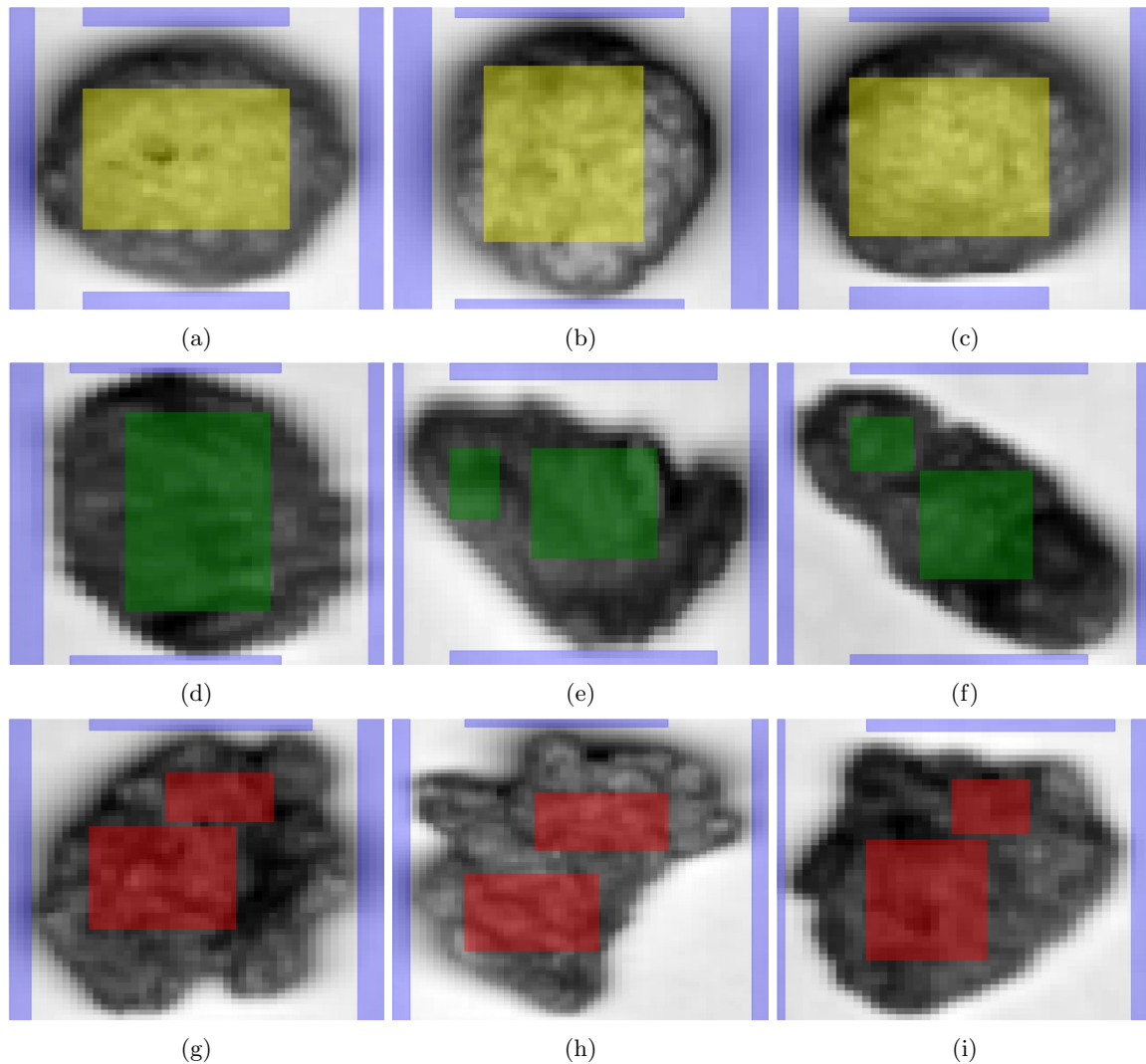


Figure 13: *Blocks of pixels (12,215 pixels of $N = 28,039$ pixels (43.5%)) selected as constraints in three greyscale images for each of the three types of synthetic puffed cereal, wheat (13a, 13b, 13c), corn (13d, 13e, 13f), and rice (13g, 13h, 13i). The pixels in the blue blocks are background, the pixels in the yellow blocks are wheat, the pixels in the green blocks are corn and the pixels in the red blocks are rice.*

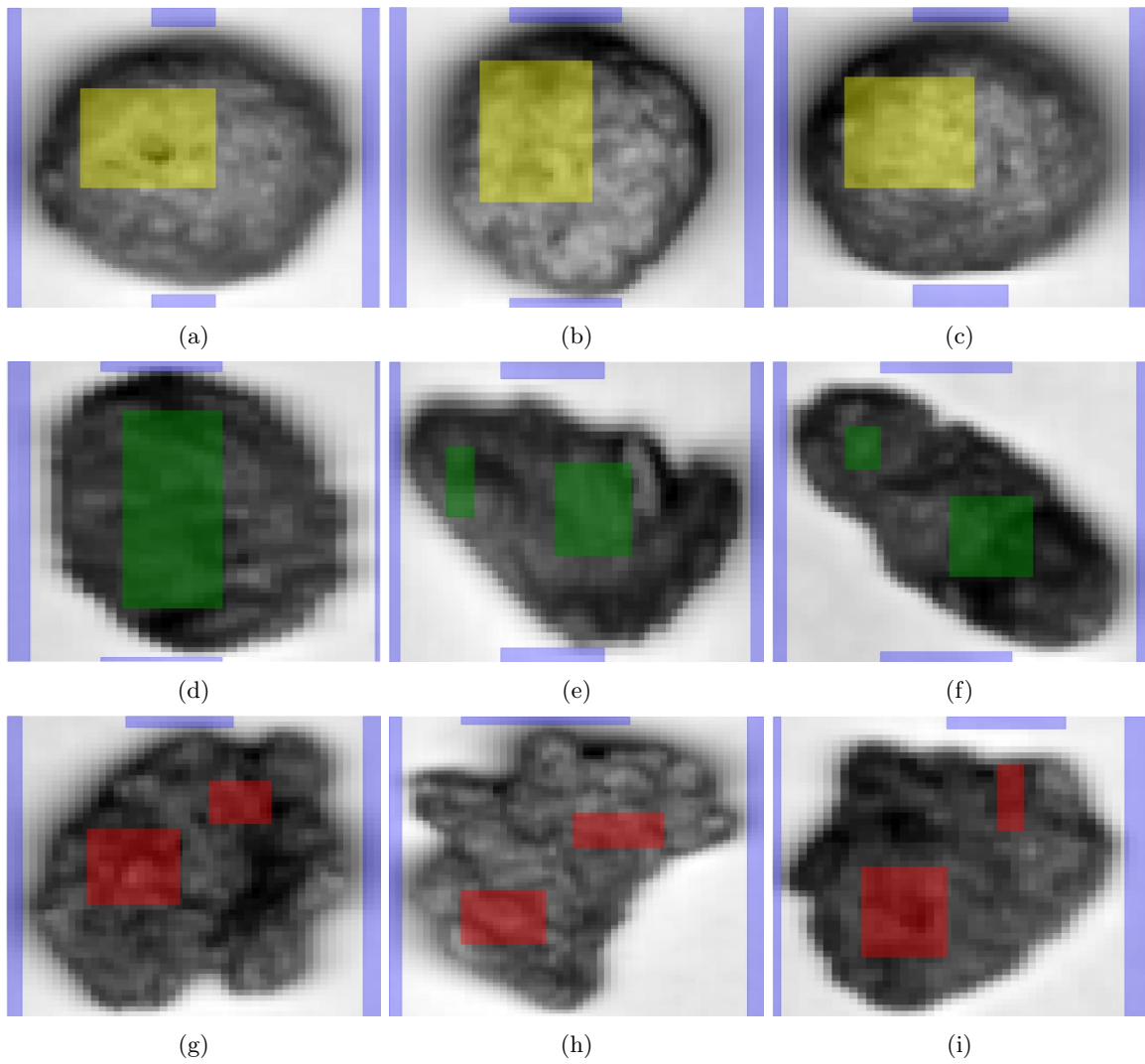


Figure 14: *Blocks of pixels (6,951 pixels of $N = 28,039$ pixels (24.7%)) selected as constraints in three greyscale images for each of the three types of synthetic puffed cereal, wheat (14a, 14b, 14c), corn (14d, 14e, 14f), and rice (14g, 14h, 14i). The pixels in the blue blocks are background, the pixels in the yellow blocks are wheat, the pixels in the green blocks are corn and the pixels in the red blocks are rice.*

11 Appendix D

As discussed in Section 4.4, Table 2 details the cumulative proportion of the variance explained by the first 5 principal components of the motivating hyperspectral image dataset.

Table 2: *Cumulative proportion of variance explained by the principal components of the motivating hyperspectral image dataset on puffed cereals.*

Number of principal components	1	2	3	4	5
Cumulative proportion of variance explained	94.2	99.7	99.92	99.94	99.95

12 Appendix E

As discussed in Section 5, Figures 15, and 16 shows the greyscale images for the remaining six hyperspectral images, and the respective pixel labels as generated using different clustering approaches.

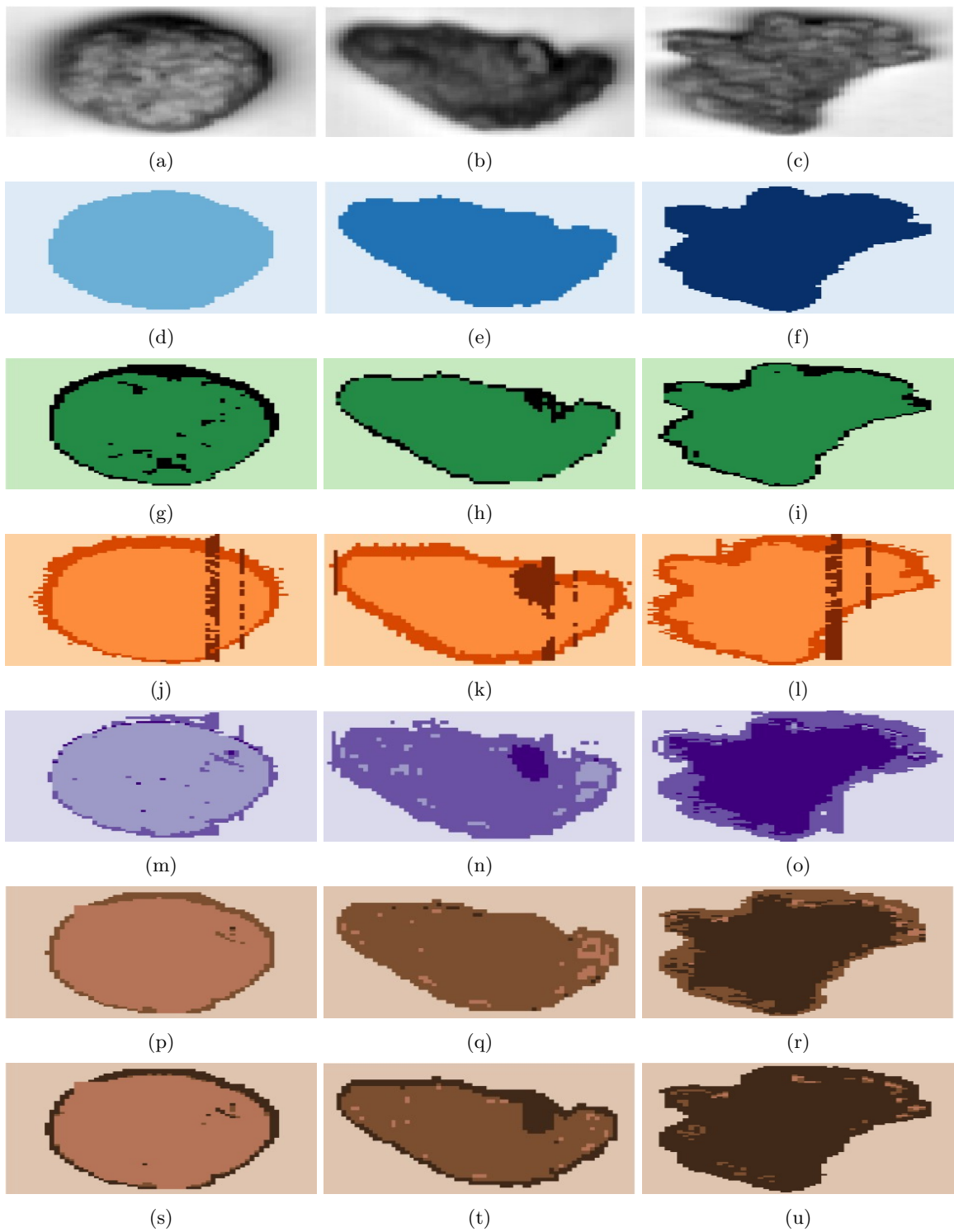


Figure 15: *Greyscale images and pixel labels for three of the nine hyperspectral images ($l = \{2, 5, 8\}$) of the cereals using the threshold approach, DBSCAN, MBC, PGMM, ccPGMM with 43.5% of pixels as constraints, and ccPGMM with 24.7% of pixels as constraints respectively for wheat (15a, 15d, 15g, 15j, 15m, 15p, 15s), corn (15b, 15e, 15h, 15k, 15n, 15q, 15t) and rice (15c, 15f, 15i, 15l, 15o, 15r, 15u).*

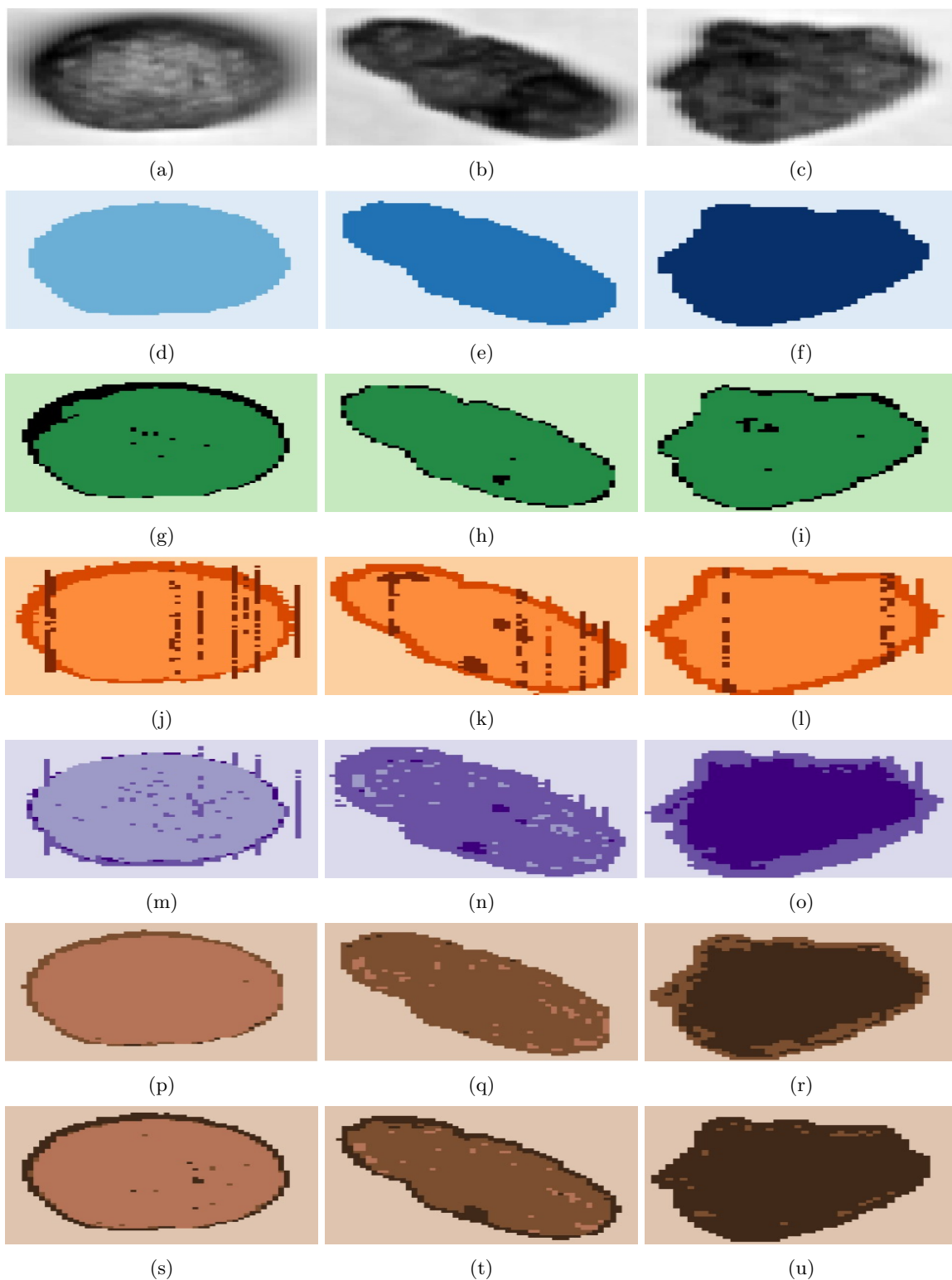


Figure 16: *Greyscale images and pixel labels for three of the nine hyperspectral images ($l = \{3, 6, 9\}$) of the cereals using the threshold approach, DBSCAN, MBC, PGMM, ccPGMM with 43.5% pixels as constraints, and ccPGMM with 24.7% pixels as constraints respectively for wheat (16a, 16d, 16g, 16j, 16m, 16p, 16s), corn (16b, 16e, 16h, 16k, 16n, 16q, 16t) and rice (16c, 16f, 16i, 16l, 16o, 16r, 16u).*

13 Appendix F

As discussed in Section 5, Figures 17, 18, and 19 illustrates the uncertainty associated with the pixel labels for the nine hyperspectral images of the puffed cereals based on the cluster solutions of MBC,

PGMM, ccPGMM with 43.5% pixels as constraints and ccPGMM with 24.7% pixels as constraints.

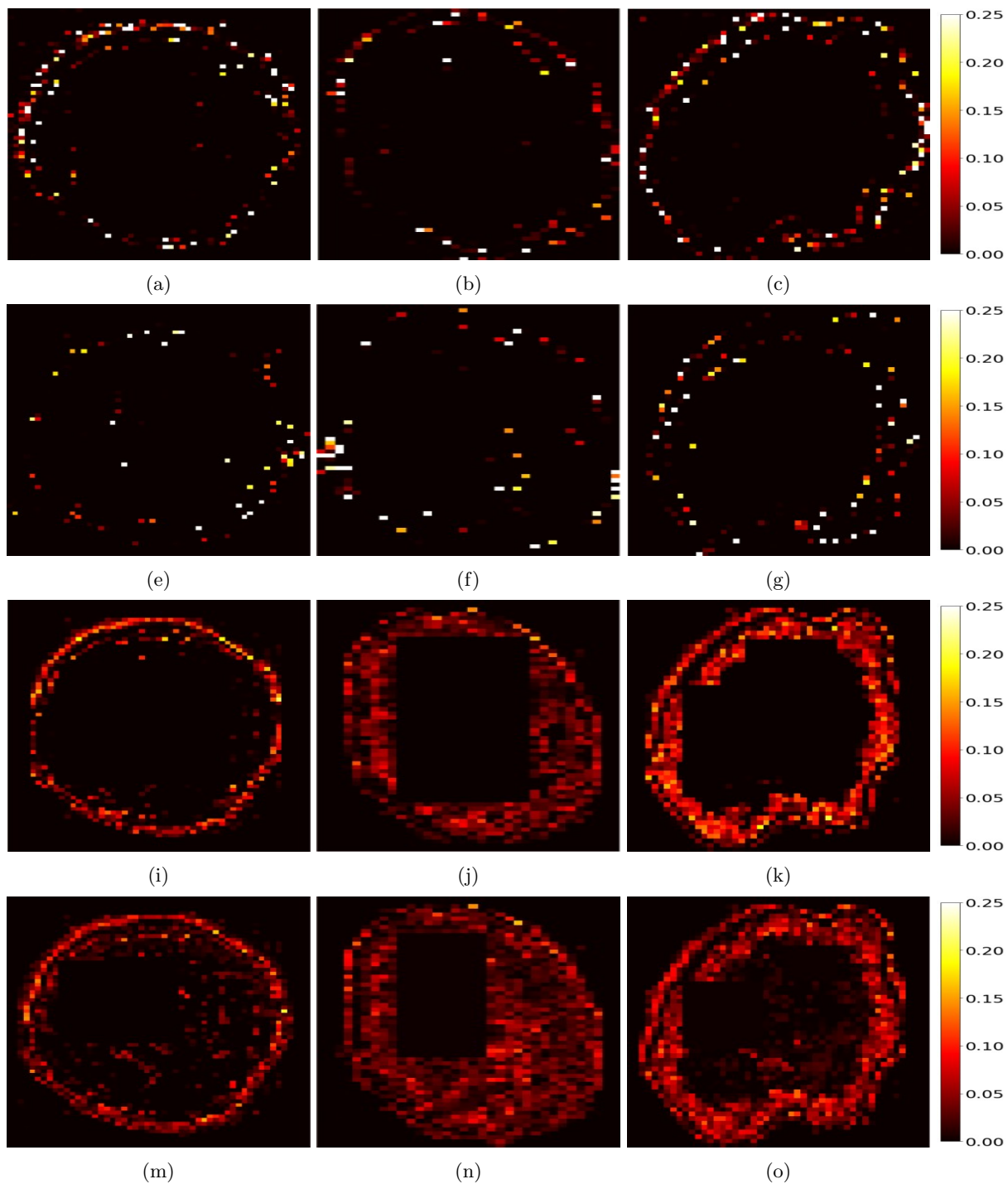


Figure 17: *Uncertainty associated with pixel labels for three of the nine hyperspectral images ($l = \{1, 4, 7\}$) of the puffed cereals based on the cluster solutions of MBC, PGMM, ccPGMM with 43.5% of pixels as constraints, and ccPGMM with 24.7% of pixels as constraints respectively for wheat (17a, 17e, 17i, 17m), corn (17b, 17f, 17j, 17n) and rice (17c, 17g, 17k, 17o).*

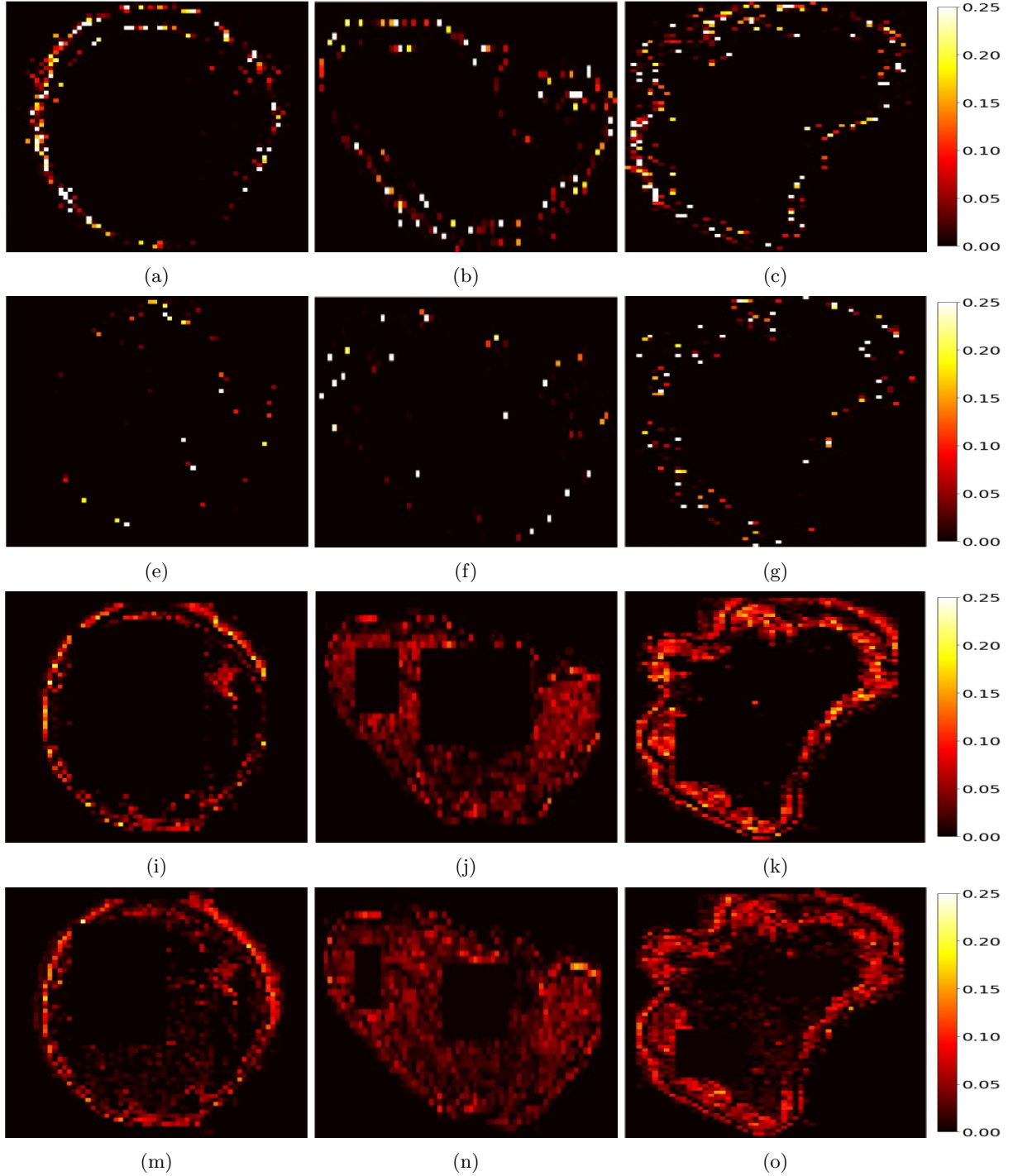


Figure 18: *Uncertainty associated with pixel labels for three of the nine hyperspectral images ($l = \{2, 5, 8\}$) of the cereals based on the cluster solutions of MBC, PGMM, ccPGMM with 43.5% of pixels as constraints, and ccPGMM with 24.7% of pixels as constraints respectively for wheat (18a, 18e, 18i, 18m), corn (18b, 18f, 18j, 18n) and rice (18c, 18g, 18k, 18o).*

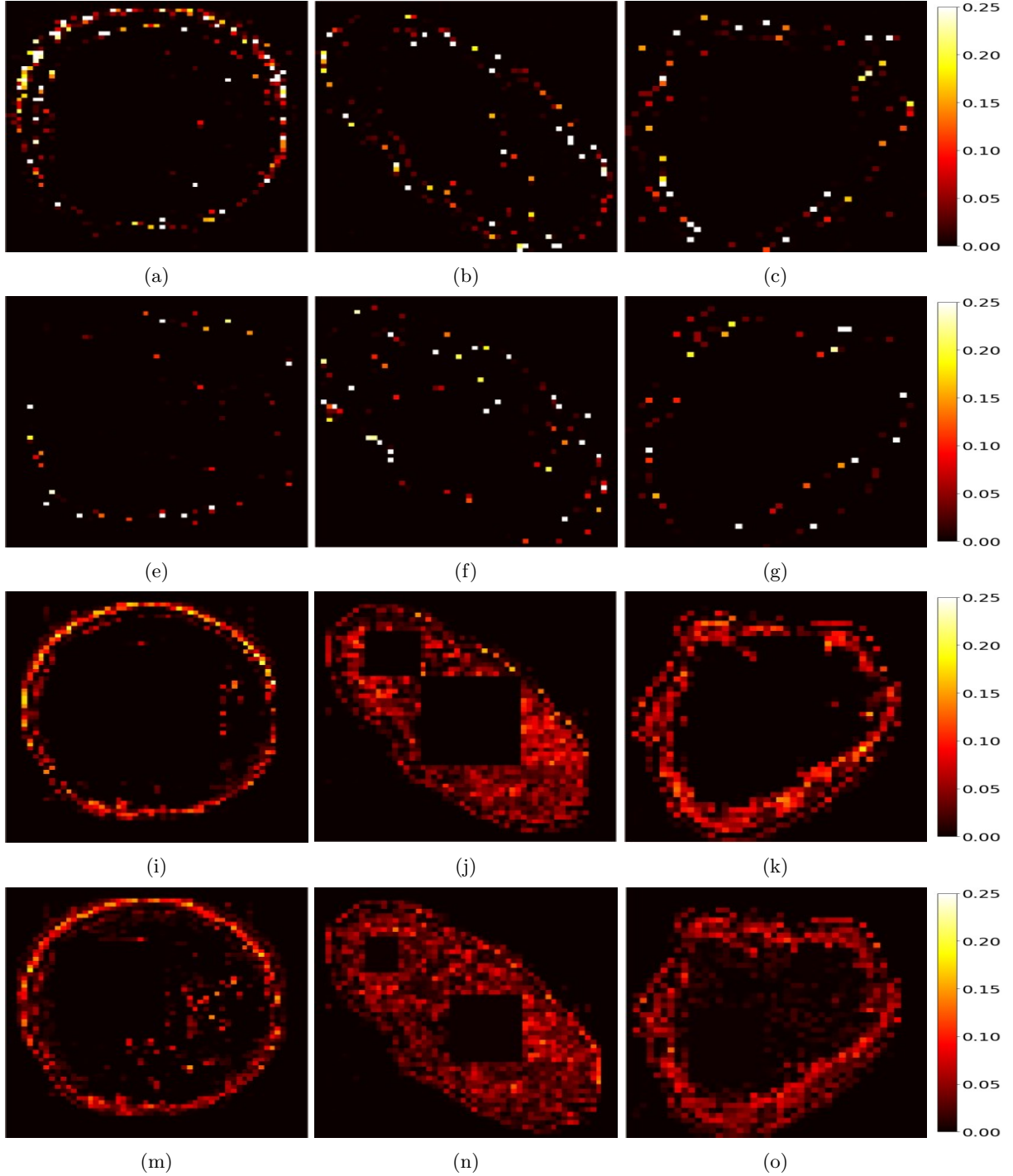


Figure 19: *Uncertainty associated with pixel labels for three of the nine hyperspectral images ($l = \{3, 6, 9\}$) of the cereals based on the cluster solutions of MBC, PGMM, ccPGMM with 43.5% of pixels as constraints, and ccPGMM with 24.7% of pixels as constraints respectively for wheat (19a, 19e, 19i, 19m), corn (19b, 19f, 19j, 19n) and rice (19c, 19g, 19k, 19o).*